國 立 交 通 大 學
材 料 科 學 與 工 程 學 系
博 士 論 文

鐵鋁鈦合金相變化

研 究 生：蘇 俊 瑋
指導教授：劉 增 豐 博士
朝 春 光 博士

中 華 民 國 九 十 六 月 八 月

Phase Transformations in Fe-Al-Ti alloys

研 究 生：蘇俊瑋　　Student: Chun-Wei Su

指導教授：劉增豐 博士　　Advisor: Prof. Tzeng-Feng Liu

朝春光 博士　　Prof. Chuen-Guang Chao

國 立 交 通 大 學

材 料 科 學 與 工 程 學 系

博 士 論 文

A Dissertation

Submitted to Department of Materials Science and Engineering

College of Engineering

National Chiao Tung University

in Partial Fulfillment of the Requirements

for the Degree of

Doctor of Philosophy

in

Materials Science and Engineering

August 2007

Hsinchu, Taiwan, Republic of China

中 華 民 國 九 十 六 年 八 月

鐵鋁鈦合金相變化

研究生：蘇 俊 瑋　　指導教授：劉 增 豐 博士

朝 春 光 博士

國立交通大學材料科學與工程研究所

中文摘要

本論文利用光學顯微鏡，掃描穿透式電子顯微鏡和 X 光能量散佈分析儀等，研究觀察不同之鋁及鈦含量對鐵-鋁-鈦三元合金顯微結構組織的影響。本論文所得到的具體研究結果如下：

(一)、當鐵-20 at.%鋁-8 at.%鈦合金經固溶處理後在 1000°C 做時效處理一小時急速淬火後，其顯微結構為 A2、$D0_3$ 與 C14 之混合相。利用穿透式電子顯微鏡及擇區繞射技術，C14 與(A2+$D0_3$) 基地之間的方向關係為:

$(0\,0\,0\,1)_{C14}//(\bar{1}\,\bar{1}\,2)_m$, $(\bar{1}\,1\,0\,0)_{C14}//(\bar{1}\,1\,0)_m$, $(1\,1\,\bar{2}\,0)_{C14}//(1\,1\,1)_m$

此方向關係至今從未被其他學者在鐵-鋁-鈦合金系統中發現過。

(二)、當鐵-23 at.%鋁-8.5 at.%鈦合金在固溶處理並急速淬火後，其顯微結構為 A2 與 $D0_3$ 之混合相。其中 A2 與 $D0_3$ 相是在淬火過程中經由 A2 →B2→(A2+$D0_3$) 規律化變態所形成的。利用穿透式電子顯微鏡檢驗發現當此合金在 900°C 做時效處理時，$D0_3$ 區域尺寸大小會隨著時效處理時間增長而變大，並且在 a/2<100>反向晶界其顯微結構

之變化依序為：A2 → (A2+$D0_3$) → (B2+$D0_3$)。此現象至今從未被其他學者在鐵-鋁-鈦合金系統中發現過。

（三）、在淬火狀態下，鐵-24.6 at.%鋁-7.5 at.%鈦合金的淬火顯微結構為 A2 與 $D0_3$ 之混合相。當此合金在 900˚C 適當時間之時效處理後，發現 $D0_3$ 區域成長，並且 B2 相會開始沿著 a/2<100>反向晶界析出。隨著時效時間的增加，$D0_3$ → (B2+$D0_3$*)相分離的現象開始發生在 a/2<100>反向晶界，並且持續相分離到先前完整的 $D0_3$ 區域。此微觀結構的變化至今從未被其他學者在鐵-鋁-鈦合金系統中發現過。

（四）、在淬火狀態下，鐵-23 at.%鋁-7 at.%鈦合金的淬火顯微結構為 A2 與 $D0_3$ 之混合相。當此合金在 800˚C 適當時間之時效處理後，$D0_3$ 區域會沿著<100>特定方向成長，並且極細微 B2 顆粒會開始在 a/2<100>反向晶界上析出。隨著時效時間的增加，B2 顆粒將會成長直到佔據整個 a/2<100>反向晶界。因此合金在 800˚C 做時效處理後其穩定顯微結構為 B2 與 $D0_3$ 之混合相。此 B2 與 $D0_3$ 形成的微觀結構發展現象至今從未被其他學者在鐵-鋁-鈦合金系統中發現過。

（五）、在淬火狀態下，鐵-20 at.%鋁-8 at.%鈦合金的淬火顯微結構為 A2 與 $D0_3$ 之混合相。此合金在 750˚C 至 1100˚C 溫度範圍內做時效處理後其微觀結構之變化依序為：A2+$D0_3$→A2+$D0_3$+C14 →B2+C14→A2+C14→A2。

Phase Transformations in Fe-Al-Ti alloys

Student: Chun-Wei Su **Advisor: Prof. Tzeng-Feng Liu**

Prof. Chuen-Guang Chao

Department of Materials Science and Engineering

National Chao Tung University

Abstract

Effects of the aluminum (Al) and titanium (Ti) contents on the phase transformations of the Fe-Al-Ti ternary alloys have been investigated by means of optical microscopy, scanning transmission electron microscopy and energy-dispersive X-ray spectrometry. On the basis of the experimental examinations, the results obtained follows:

[1]. When the Fe-20at.%Al-8at.%Ti alloy was aged at 1000˚C for 1 h and then quenched, the microstructure of the alloy was a mixture of (A2+$D0_3$+C14) phases. By means of transmission electron microscopy and diffraction technique, the orientation relationship between the C14 precipitate and (A2+$D0_3$) matrix was determined as follows:

$(0\,0\,0\,1)_{C14}//(\bar{1}\,\bar{1}\,2)_m$, $(\bar{1}\,1\,0\,0)_{C14}//(\bar{1}\,1\,0)_m$, $(1\,1\,\bar{2}\,0)_{C14}//(1\,1\,1)_m$.

The present result of the orientation relationship has never been reported by previous workers in the Fe-Al-Ti alloy systems before.

[2]. The as-quenched microstructure of the Fe-23 at.% Al-8.5 at.% Ti alloy was a mixture of (A2+$D0_3$) phases. Transmission electron microscopy (TEM) examinations indicated that when the alloy was aged at 900˚C, the size of the $D0_3$ domains increased with increasing the aging time, and an A2 → (A2+$D0_3$) → (B2+$D0_3$) transition occurred at a/2<100> anti-phase boundaries (APBs). This feature has never been reported by other workers in the Fe-Al-Ti alloy systems before.

[3]. The as-quenched microstructure of the Fe-24.6 at.% Al-7.5 at.% Ti alloy was a mixture of (A2+$D0_3$) phases. When the alloy was aged at 900˚C for moderate times, the $D0_3$ domains grew considerably and B2 phase appeared on a/2<100> anti-phase boundaries (APBs). With continued aging at 900˚C, phase separation from prior-$D0_3$ to (B2+$D0_3$*) occurred initially on a/2<100> APBs, and then proceeded toward the whole prior-$D0_3$ domains. This microstructural revolution has never been reported by other workers in the Fe-Al-Ti alloy systems before.

[4]. The as-quenched microstructure of the Fe-23 at.% Al-7 at.% Ti alloy was a mixture of (A2+$D0_3$) phases. When the as-quenched alloy was aged at 800˚C for moderate times, the $D0_3$ domains grew preferentially along <100> crystallographic directions and extremely

fine B2 particles started to occur at a/2<100> anti-phase boundaries (APBs). After prolonged aging at 800˚C, the B2 particles would grow to occupy the whole a/2<100> APBs. Consequently, the stable microstructure of the alloy at 800˚C was a mixture of (B2+$D0_3$) phases. The microstructural development for the formation of the (B2+$D0_3$) phases has never been reported in Fe-Al-Ti alloy systems before.

[5]. As-quenched microstructure of the Fe-20 at.% Al-8 at.% Ti alloy was a mixture of (A2+$D0_3$) phases. When the as-quenched alloy was aged at temperatures ranging from 750˚C to 1100˚C, the phase transition sequence as the aging temperature increased was found to be A2+$D0_3$→A2+$D0_3$+C14→B2+C14→A2+C14→A2. It is noted here that the phase transition has never been observed by other workers in the Fe-Al-Ti alloys before.

Contents

List of Tables

List of Figures

Chapter 1.

General Introduction

General Introduction

Fe-rich section of the Fe-Al binary alloy has mainly three equilibrium phases, namely disordered A2, ordered B2 (FeAl) and ordered $D0_3$ (Fe_3Al), as shown in Figure 1.1 [1-3]. All these three phases have the same basically body-centered cubic (BCC) crystal structure. Fe-Al alloys are favorable for applications as high temperature structural application because of their low cost, reasonable strength and good corrosion resistance [3-5]. However, these have been very limited due to their low room-temperature ductility and a sharp drop in strength above 600˚C, which is well-known to be related to the $D0_3 \rightarrow B2$ phase transformation [3]. In order to improve the high temperature strength, addition of alloying elements as transition metals (Ti, V, Mo, Zr…etc.) was shown to increase transition temperature significantly over that for the Fe-Al binary alloys. Especially, the addition of titanium resulted in a particularly large increase of the $D0_3 \rightarrow B2$ transition temperature about 60˚C/at.% [6-10].

The effects of titanium addition on the microstructures of the Fe-Al binary alloys have also been studied by many workers [10-22]. Based on these results, it is concluded that the titanium addition in the Fe-Al binary alloys would (1) strongly increase the $D0_3 \rightarrow B2$ transition temperature, (2) significantly expand the ($A2+D0_3$) phase field, and (3) cause the $D0_3$

anti-phase boundaries (APBs) to exhibit a tendency toward anisotropy [16-21]. Moreover, titanium preferentially substitutes for Fe at a specific lattice site with eight nearest Fe atoms (4(b) sites) rather than a site with four Fe and four Al nearest atoms (8(c) sites) in $D0_3$ structure [10], as shown in Figure 1.2. This implies that Fe_2AlTi is a Heusler phase ($L2_1$) and not $(Fe,Ti)_3Al$ ($D0_3$). The FeAl (B2) phase also dissolves a significant amount of titanium leading to increase in lattice parameter [23].

In 1987, M.G. Mendiratta *et al.* first reported that the order-disorder transitions concerning about A2, B2 and $D0_3$ phases using five Fe-(17.3 ~ 25.2) at.% Al-(4.4 ~ 5.2) at.% Ti alloys [18]. In their study, it was reported that addition of about 5 at.% Ti shifted the (A2+$D0_3$) phase field to higher temperature and to lower Al content compared to Fe-Al binary alloys by using transmission electron microscopy (TEM) investigations [18]. Recently, in 2006, Palm *et al.* determined complete isothermal sections of the Fe-Al-Ti ternary alloys at 800˚C~1000˚C, as shown in Figure 1.3 [15]. In their phase diagrams, it was found that the A2 single phase-field exists in the composition triangle spanned by the composition lines FeAl-Fe_3Al, Fe_3Al-Fe_2AlTi and Fe_2AlTi-FeAl. The phase equilibria were determined by optical micrography (OM), scanning electron microscopy (SEM), electron-probe microanalysis (EPMA) and X-ray diffraction (XRD). More

recently, Ohnuma *et al.* claimed that two kinds of phase separations ($A2+D0_3$) and ($B2+D0_3$) were observed in the composition range below 25 at.% Al by using EPMA [19-21]. The width of the two-phase region violently increases with decreasing Al composition, as shown in Figure 1.4.

Based on the above studies, it is seen that only five phase fields, namely A2, $A2+D0_3$, $D0_3$, ($D0_3$+B2) and B2, could be found in the Fe-rich Fe-Al-Ti ternary alloys. It is worthy mentioning that the ($B2+D0_3$) two-phase field has not been found by previous workers in the Fe-Al binary alloys before [19-21]. However, when the Ti content was increased to 7 at.% or above, C14 precipitates could be investigated to form within the B2 or A2 matrix in the aged Fe-Al-Ti alloys [13-15,23-24]. The C14 precipitate has a hexagonal structure with lattice parameters a=0.5038 nm and c=0.8193 nm [23]. It is worthy mentioning that the C14 precipitate was also observed by many workers in Fe-Al-Nb, Fe-Al-Zr and Fe-Al-Ta alloys [17,25-26]. However, we are aware of only one article, in which the orientation relationship between the C14 precipitate and A2 matrix was predicted. In 2005, Morris *et al.* reported that when the Fe-25Al-2Nb alloy was aged at 800˚C or 900˚C, C14 precipitates were formed within the A2 matrix; the orientation relationship between the C14 precipitate and A2

matrix was $\{\bar{1}\,0\,1\,0\}_{C14} // \{\bar{1}\,0\,1\}_m$, $\langle 1\,\bar{2}\,1\,0\rangle_{C14} \approx \langle 0\,1\,0\rangle_m$ and $\langle 0\,0\,0\,1\rangle_{C14} \approx \langle 1\,0\,1\rangle_m$, which was determined by using two SADPs [25]. Although the C14 precipitate was extensively reported to be detected in the aged Fe-Al-Ti alloys, little information concerning the orientation relationship between the C14 precipitate and matrix has been provided.

In order to further clarify the ambiguous orientation relationship, a transmission electron microscopy study was performed to determine the orientation relationship between C14 precipitate and A2 matrix in an Fe-20at.% Al-8at.% Ti alloy. The detailed experimental results and discussion are presented in Chapter 2.

Additionally, up to now, the existence of the (B2+$D0_3$) two-phase field in the Fe-Al-Ti ternary alloys was confirmed principally by using XRD and EPMA. Little TEM information concerning the microstructural revolution for the formation of (B2+$D0_3$) phases has been provided. Therefore, an attempt to investigate the microstructural revolution for the formation of (B2+$D0_3$) phases in the Fe-Al-Ti alloys were performed by using TEM and energy dispersive X-ray spectrometer (EDS) analyses. The detailed experimentally results are presented in Chapters 3 through 5, respectively.

References

1. P.R. Swann, W.R. Duff, R.M. Fisher, Metall. Trans. 3 (1972) 409..
2. S.M. Allen, J.W. Cahn, Acta Metall. 24 (1976) 425.
3. O. Ikeda, I.Ohnuma, R. Kainuma, K. Ishida: Intermetallics 9 (2001) 755.
4. D.G. Morris, M. Leboeuf, S. Gunther, M. Nazmy, Phil Mag A70:1067.
5. C.G. McKamey, J.H DeVan, P.F. Tortorell, V.K. Sikka, J Mater Res 6 (1991) 1779.
6. J. M. Cairney, P.R. Munroe, J. Mater. Sci. Let. 18 (1999) 449.
7. U. Prakash, R.A. Buckley, H. Jones, Mater. Sci. Tech. 9 (1993) 16.
8. Y. Nishino, C. Kumada, S. Asano, Scripta Mater. 36 (1997) 461.
9. Y. Nishino, S. Asano, T. Ogawa, Mater. Sci. Eng. A 234-236 (1997) 271.
10. L. Anthony, B. Fultz, Acta Metall. Mater. 43 (1995) 388.
11. F. Dobeš, P. Kratochvíl, K. Milička, Intermetallics 14 (2006) 1199.
12. S.M. Zhu, K. Sakamoto, M. Tamura, K. Iwasaki, Scripta Mater. 42 (2000) 905.
13. U. Prakash, G. Sauthoff, Intermetallics 9 (2001) 107.
14. M. Palm, G. Sauthoff, Intermetallics 12 (2004) 1345.
15. M. Palm, J. Lacaze, Intermetallics 14 (2006) 1291.

16. F. Stein, A. Schneider, G. Frommeyer, Intermetallics 11 (2003) 71.

17. M. Palm, Intermetallics 13 (2005) 1286.

18. M.G. Mediratta, S.K. Ehlers, H.A. Lipsitt, Metall. Trans. A 18 (1987) 509.

19. G. Ghosh, in: G. Effenberg (Eds.), Ternary Alloy Systems, Springer Berlin Heidelberg, New York, 2005, pp. 426-452.

20. I. Ohnuma, C.G. Schön, R. Kainuma, G. Inden, K. Ishida, Acta Mater. 46 (1998) 2083.

21. S.M. Zhu, K. Sakamoto, M. Tamura, K. Iwasaki, Mater. Trans. JIM. 42 (2001) 484.

22. O. Ikeda, I. Ohnuma, R. Kainuma, K. Ishida, Intermetallics 9 (2001) 755.

23. M. Palm, G. Inden, N. Thomas, J. Phase Equilibria 16 (1995) 209.

24. C.H. Sellers, T.A. Hyde, T.K. O'Brien, R.N. Wright, J. Phys. Chem. Solids 55 (1994) 505.

25. D.G. Morris, L.M. Requejo, M.A. Muñoz-Morris, Intermetallics 13 (2005) 862.

26. F. Stein, M. Palm, G. Sauthoff, Intermetallics 13 (2005) 1056.

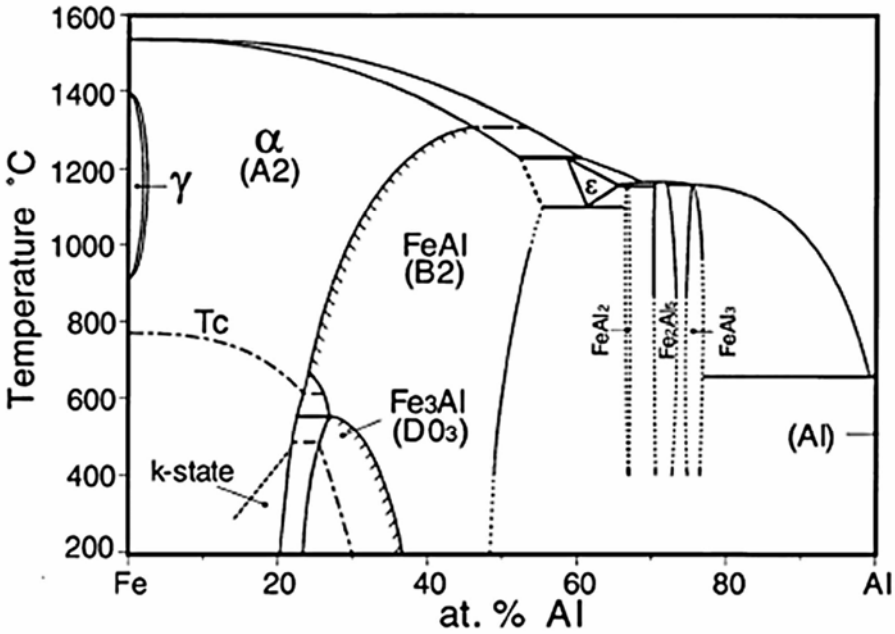

Figure 1.1 Fe-Al binary alloy phase diagram.

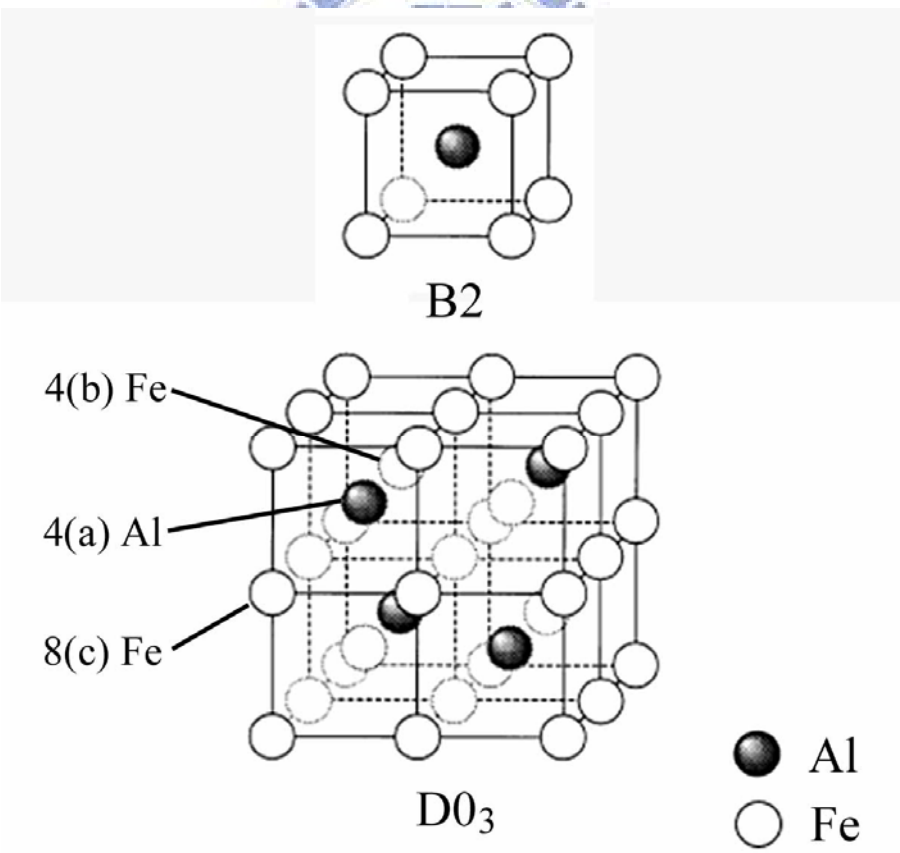

Figure 1.2 crystal structures of B2 and $D0_3$.

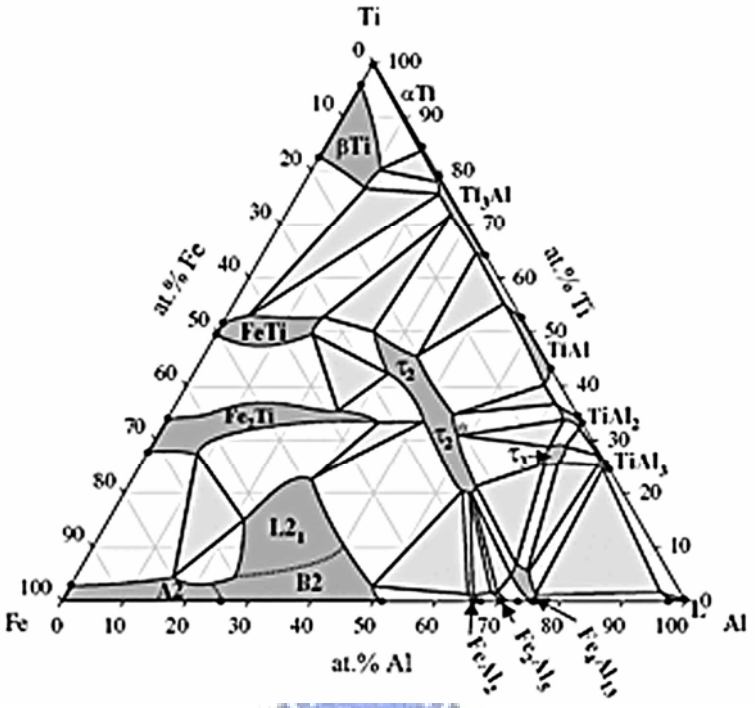

Figure 1.3 (a)

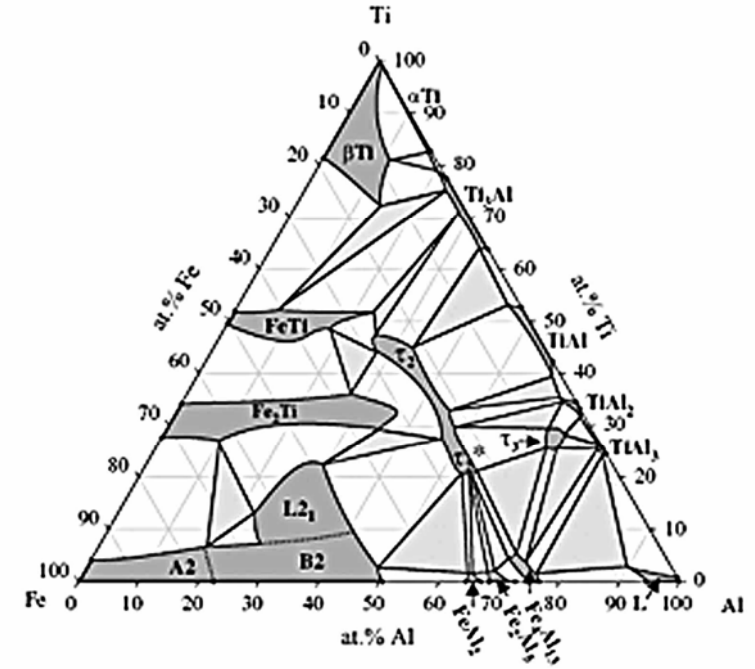

Figure 1.3 (b)

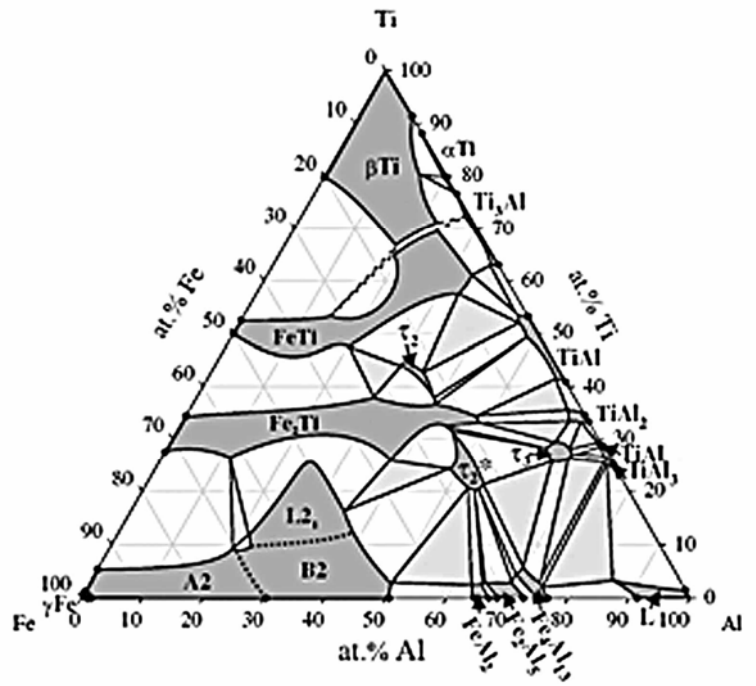

Figure 1.3 (c)

Figure 1.3 Isothermal section of the Fe-Al-Ti ternary alloy at (a) 800˚C, (b) 900˚C and (c) 1000˚C, respectively.

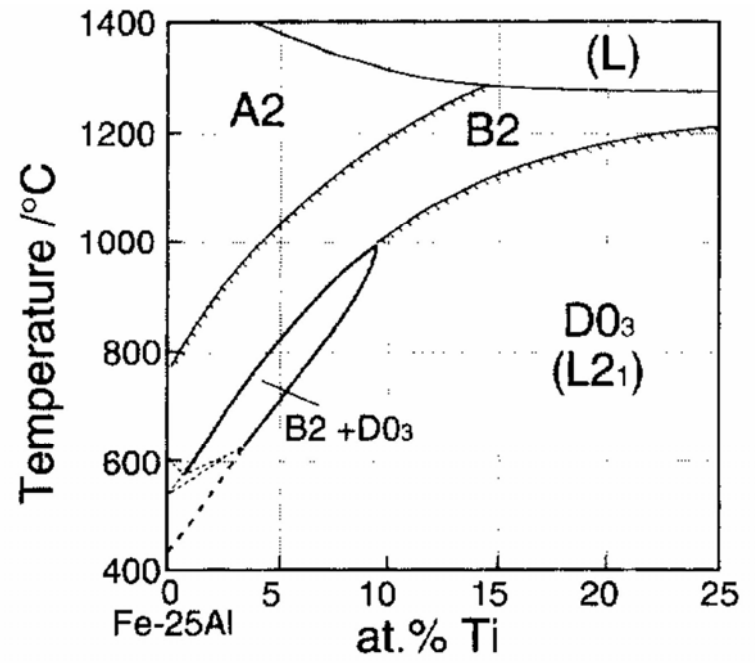

Figure 1.4 (a)

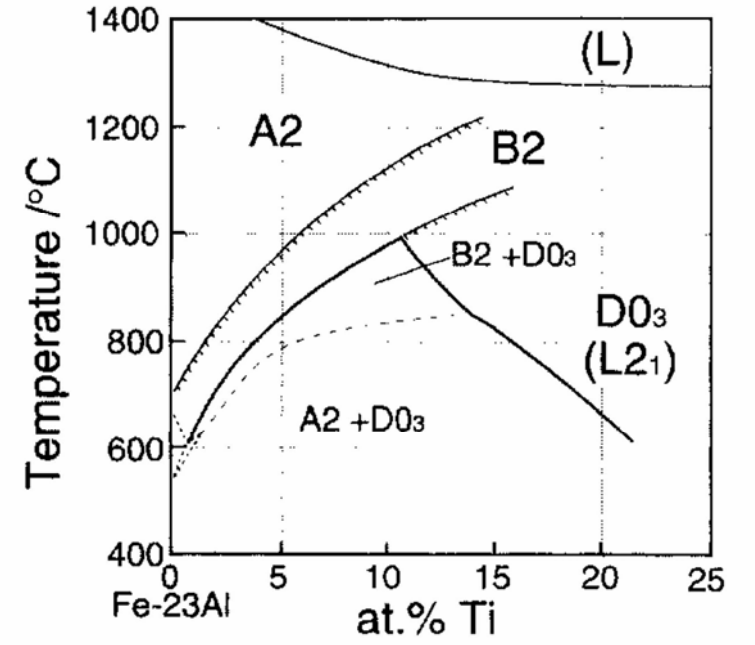

Figure 1.4 (b)

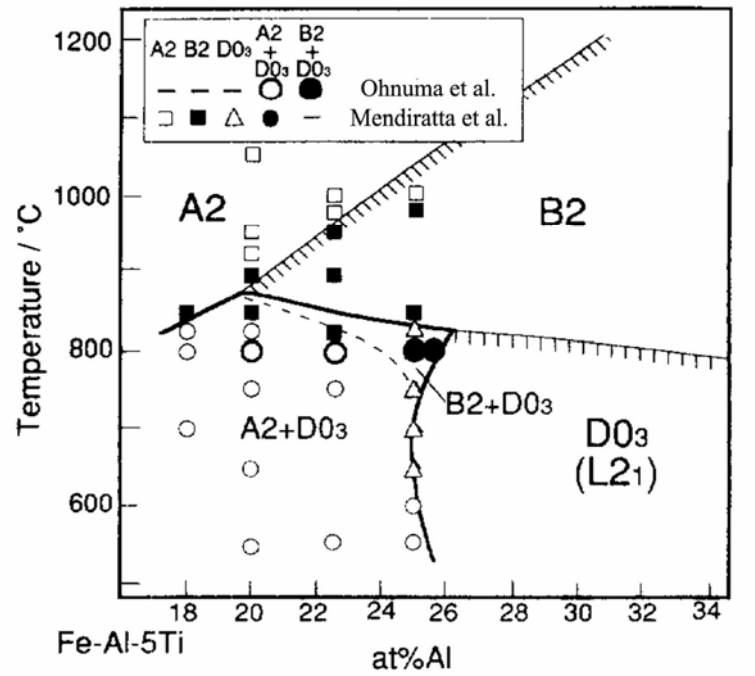

Figure 1.4 (c)

Figure 1.4 (a)-(b) Vertical sections at constant Al content. (a) 25 at.% Al, and (b) 23 at.% Al, respectively. (c) vertical section at constant 5 at.% Ti.

Chapter 2.

Orientation relationship between C14 precipitate and ferrite matrix in an Fe-20 at.% Al-8 at.% Ti alloy

Orientation relationship between C14 precipitate and ferrite matrix in an Fe-20 at.% Al-8 at.% Ti alloy

Abstract

C14 precipitates were observed to appear within the ferrite matrix in the Fe-20 at.% Al-8 at.% Ti alloy aged at 1000˚C. By means of transmission electron microscopy and diffraction techniques, the orientation relationship between the C14 precipitate and ferrite matrix was determined as follows: $(0\,0\,0\,1)_{C14}//(\bar{1}\,\bar{1}\,2)_m$, $(\bar{1}\,1\,0\,0)_{C14}//(\bar{1}\,1\,0)_m$, $(1\,1\,\bar{2}\,0)_{C14}//(1\,1\,1)_m$. The present result of the orientation relationship between the two phases has never been reported by previous workers in the Fe-Al-Ti alloy systems before.

2-1 Introduction

The microstructures of the Fe-Al-Ti alloys have been studied by other workers [1-6]. In their studies, it is seen that only four phase fields, namely A2 (ferrite), A2+$D0_3$, $D0_3$ and B2, could be found in the Fe-(18~25) at.% Al-Ti alloys with Ti≦5 at.% [1,2]. However, when the Ti content was increased to 7 at.% or above, C14 precipitates could be investigated to form within the B2 or A2 matrix in the aged Fe-Al-Ti alloys [2-6]. The C14 precipitate has a hexagonal structure with lattice parameters a=0.5038 nm and c=0.8193 nm [6]. Although the C14 precipitate was extensively reported to be detected in the aged Fe-Al-Ti alloys, little information concerning the orientation relationship between the C14 precipitate and matrix has been provided. Therefore, the purpose of the present study is an attempt to determine the orientation relationship between the C14 precipitate and A2 matrix in the Fe-20 at.% Al-8 at.% Ti alloy.

2-2 Experimental procedure

The Fe-20 at.% Al-8 at.% Ti alloy was prepared in a vacuum induction furnace by using 99.9% Fe, 99.9% Al and 99.9% Ti. The melt was chill cast into a 30 × 50 × 200-mm-copper mold. After being homogenized at 1250˚C for 48 h, the ingot was sectioned into 2-mm-thick slices. These slices were subsequently solution heat-treated at 1250˚C for 2 h and then quenched into room-temperature water rapidly. The aging processes were performed at 1000˚C for various times in a vacuum heat-treated furnace and then quenched rapidly. TEM specimens were prepared by means of double-jet electropolisher with an electrolyte of 67% methanol and 33% nitric acid. The polishing temperature was kept in the range from -30˚C to -20˚C, and the current density was kept in the range from 4.0×10^4 to 6.0×10^4 A/m^2. Electron microscopy was performed on a JEOL JEM-2000FX scanning transmission electron microscope operating at 200kV.

2-3 Results and discussion

Figure 2.1(a) is a bright-field (BF) electron micrograph of the as-quenched alloy. Figure 2.1(b) is a selected-area diffraction pattern (SADP) of the as-quenched alloy, exhibiting the superlattice reflection spots of the ordered $D0_3$ phase [7]. Figure 2.1(c) is a $(\bar{1}11)$ $D0_3$ dark-field (DF) electron micrograph of the as-quenched alloy, revealing the presence of extremely fine $D0_3$ domains. Figure 2.1(d), a (002) DF electron micrograph, shows the presence of small B2 domains and a high density of disordered A2 phase (dark contrast) within the B2 domains. Since the sizes of both $D0_3$ and B2 domains are very small, it is deduced that the (A2+$D0_3$) phases existing in the as-quenched alloy were formed by an A2→B2→(A2+$D0_3$) ordering transition during quenching. This result is similar to that observed by other workers in the Fe-(18~22.5) at.% Al-5 at.% Ti alloys [1].

When the as-quenched alloy was aged at 1000˚C for moderate times, some plate-like precipitates started to appear within the matrix. A typical example is shown in Figure 2.2(a). Figures 2.2(b) and (c) are the $(\bar{1}11)$ and (002) $D0_3$ DF electron micrographs taken from the same area as Figure 2.2(a), indicating the existence of the small quenched-in $D0_3$ and B2 domains, respectively. Figures 2.2(d) through (f) show three different

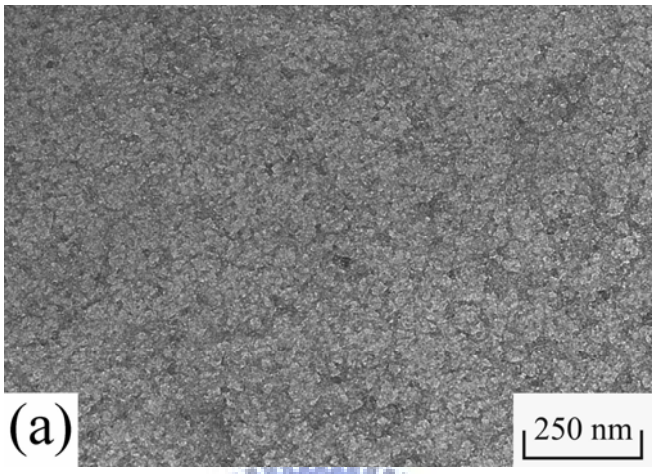

Figure 2.1 (a)

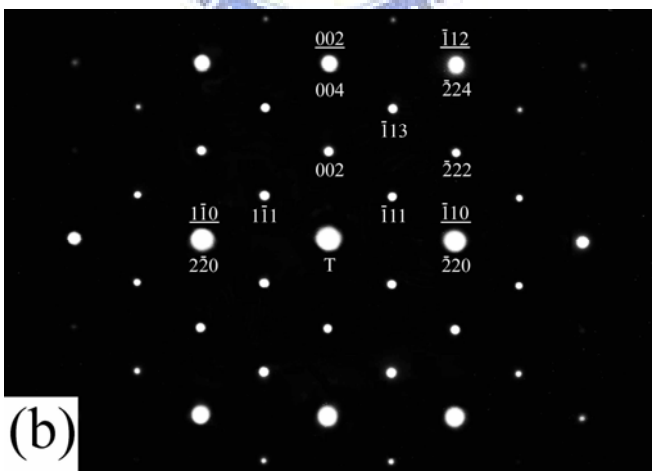

Figure 2.1 (b)

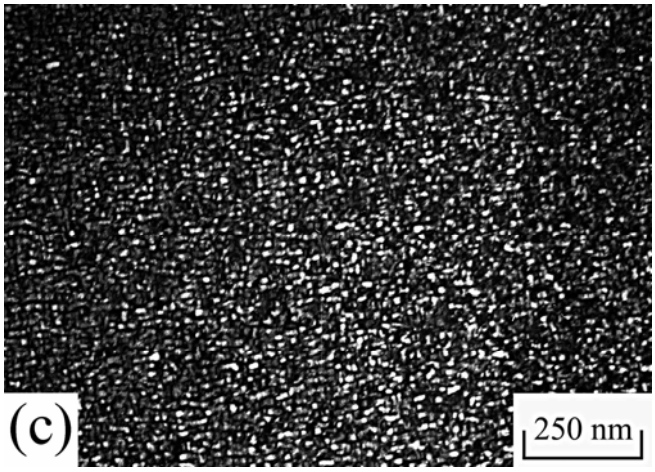

Figure 2.1 (c)

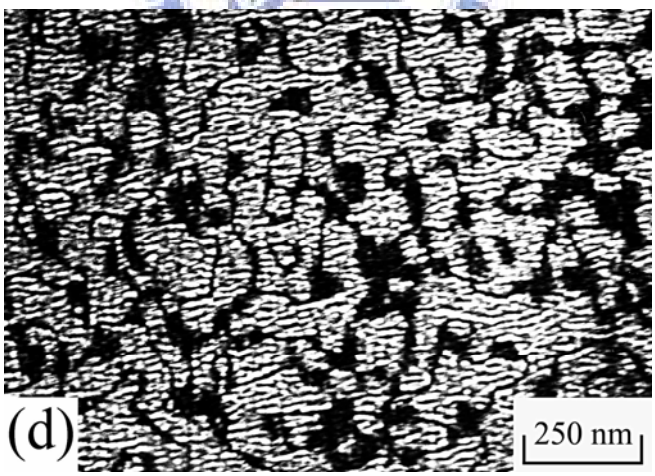

Figure 2.1 (d)

Figure 2.1 Electron micrographs of the as-quenched alloy: (a) BF, (b) an SADP. The foil normal is $[1\ 1\ 0]$. (<u>hkl</u> = ferrite phase; hkl = $D0_3$ phase.), (c) and (d) $(\bar{1}11)$ and (002) $D0_3$ DF, respectively.

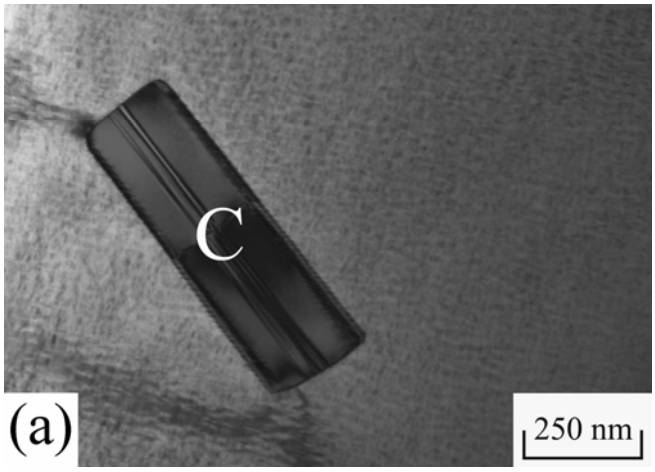

Figure 2.2 (a)

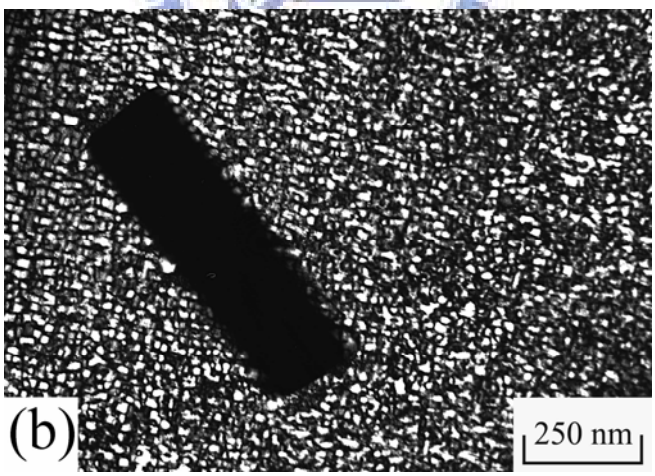

Figure 2.2 (b)

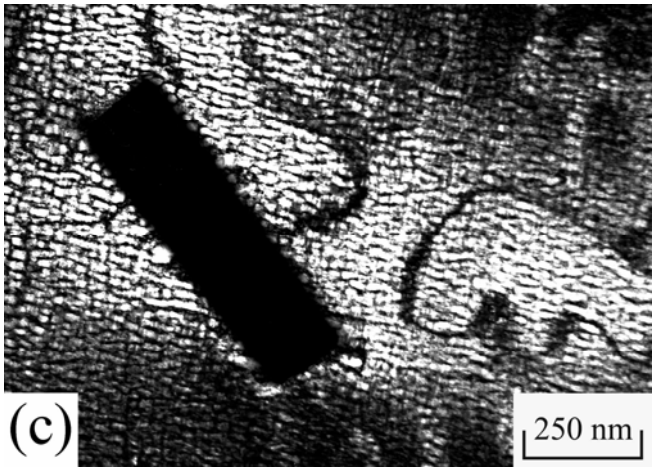

Figure 2.2 (c)

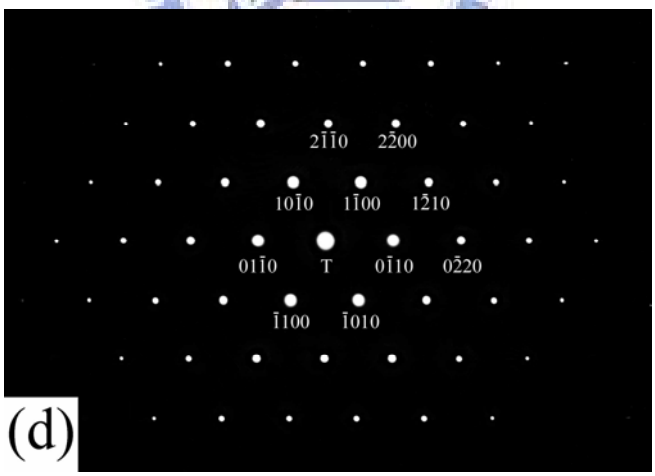

Figure 2.2 (d)

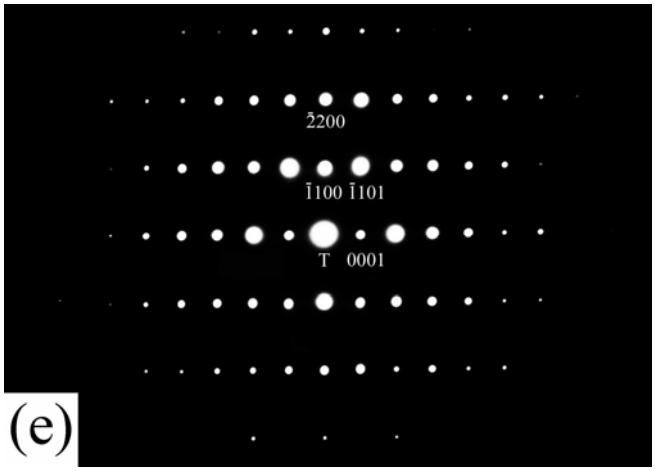

Figure 2.2 (e)

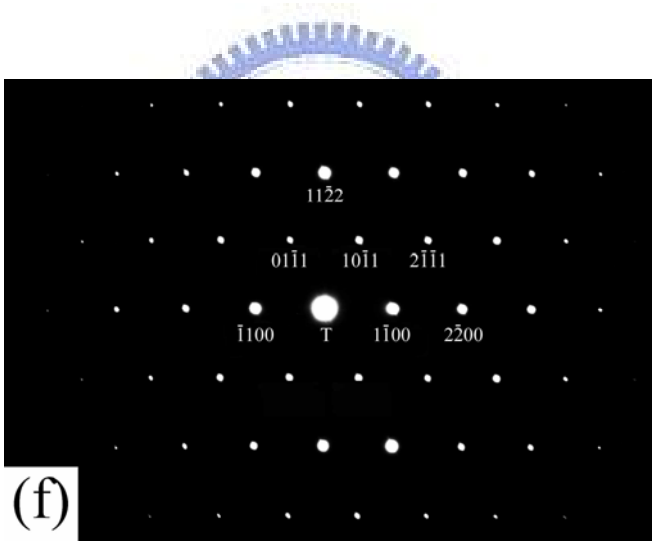

Figure 2.2 (f)

Figure 2.2 Electron micrographs of the alloy aged at 1000˚C for 1 h: (a) BF, (b) and (c) $(\bar{1}11)$ and (002) $D0_3$ DF, respectively. , (d) through (f) three SADPs taken from the precipitate marked as "C" in (a). The zone axes of the C14 precipitate are (d) $[0\ 0\ 0\ 1]$, (e) $[1\ 1\ \bar{2}\ 0]$ and (f) $[1\ 1\ \bar{2}\ \bar{3}]$, respectively.

SADPs taken from the plate-like precipitate marked as “C” in Figure 2.2(a). According to the camera length and the measurement of d-spacings as well as angles among the reciprocal lattice vectors of the diffraction spots, the crystal structure of the precipitate was determined to be hexagonal with lattice parameters a=0.505 nm and c=0.801 nm, which corresponds to that of the C14 phase [6]. The zone axes of the precipitate in Figures 2.2(d) through (f) are $[0\,0\,0\,1]$, $[1\,1\,\bar{2}\,0]$ and $[1\,1\,\bar{2}\,\bar{3}]$, respectively. Based on the above examinations, it is concluded that the microstructure of the alloy present at 1000˚C should be a mixture of (A2+C14) phases.

In order to determine the orientation relationship between the C14 precipitate and the (A2+$D0_3$) matrix, ten different SADPs were taken from an area including the precipitate marked as “C” in Figure 2.2(a) and its surrounding (A2+$D0_3$) phases. The results are shown in Figures 2.3(a) through (j). These SADPs were obtained by tilting the specimen about some specific reflections. Table 2.1 shows the interplanar spacings of the C14 precipitate, which were measured directly from the SADPs in Figure 2.3(a) through (j). The measured angles among the reciprocal lattice vectors and the calculated interplanar angles are listed in Table 2.2. Based on the lattice parameters *a* = 0.505 nm, *c* = 0.801 nm determined

in the above paragraph, the corresponding indices of these diffraction spots and the angles between the chosen reciprocal reflection are determined and calculated by using the following equations: [8]

$$\frac{1}{d^2} = \frac{4}{3a^2}\left(h^2 + hk + k^2\right) + \frac{l^2}{c^2} \qquad (1)$$

$$\cos\phi = \frac{h_1h_2 + k_1k_2 + \frac{1}{2}\left(h_1k_2 + k_1h_2\right) + \frac{3a^2}{4c^2}l_1l_2}{\left\{\left(h_1^{\,2} + k_1^{\,2} + h_1k_1 + \frac{3a^2}{4c^2}l_1^{\,2}\right)\left(h_2^{\,2} + k_2^{\,2} + h_2k_2 + \frac{3a^2}{4c^2}l_2^{\,2}\right)\right\}^{\frac{1}{2}}} \qquad (2)$$

For comparison, the calculated interplanar spacings and the angles are also listed in Tables 2.1 and 2.2. It can be seen in Tables 2.1 and 2.2 that the measured values are quite consistent with those obtained by calculation. Consequently, the zone axes of the C14 precipitate and (A2+D0$_3$) matrix in Figures 2.3(a) through (j) are $[1\,1\,\bar{2}\,0]_{C14}$, $[1\,1\,1]_m$; $[2\,2\,\bar{4}\,\bar{3}]_{C14}$, $[1\,1\,0]_m$; $[5\,5\,\overline{10}\,\overline{12}]_{C14}$, $[\bar{3}\,\bar{3}\,1]_m$; $[1\,1\,\bar{2}\,\bar{3}]_{C14}$, $[\bar{2}\,\bar{2}\,1]_m$; $[1\,1\,\bar{2}\,\bar{6}]_{C14}$, $[\bar{1}\,\bar{1}\,1]_m$; $[0\,0\,0\,1]_{C14}$, $[\bar{1}\,\bar{1}\,2]_m$; $[7\,1\,\bar{8}\,\bar{6}]_{C14}$, $[2\,1\,0]_m$; $[13\,\bar{5}\,\bar{8}\,\bar{6}]_{C14}$, $[1\,0\,0]_m$; $[7\,\bar{2}\,\bar{5}\,\bar{6}]_{C14}$, $[\bar{5}\,\bar{1}\,1]_m$ and $[5\,\bar{1}\,\bar{4}\,\bar{6}]_{C14}$, $[\bar{3}\,\bar{1}\,1]_m$, respectively. For better demonstration, higher magnification of Figures 2.3(a), (b), (f) and (h) is shown in Figures 2.4(a) through (d), respectively. It is obvious in Figures 2.4(a) and (c) that the $(0\,0\,0\,1)$ and $(1\,1\,\bar{2}\,0)$ reflection spots of the C14 precipitate are nearly parallel to the $(\bar{1}\,\bar{1}\,2)$

and $(1\,1\,1)$ reflection spots of the matrix, respectively. By means of this information, a stereographic plot of poles (superimposing the $(0\,0\,0\,1)$ projection of the C14 precipitate and the $(\bar{1}\,\bar{1}\,2)$ projection of the matrix) was constructed, as shown in Figure 2.5, where the $(1\,1\,\bar{2}\,0)$ pole of the C14 precipitate was made to match with the $(1\,1\,1)$ pole of the A2 matrix. In the meantime, the angles among the chosen zone axes for the cubic and hexagonal structure, as shown in Figure 2.3(a) through (j), were also calculated and listed in Table 2.3 by the following equations : [8]

Cubic : $$\cos\rho = \frac{u_1u_2 + v_1v_2 + w_1w_2}{\left\{\left(u_1^{\,2} + v_1^{\,2} + w_1^{\,2}\right)\left(u_2^{\,2} + v_2^{\,2} + w_2^{\,2}\right)\right\}^{\frac{1}{2}}} \tag{3}$$

HCP : $$\cos\phi = \frac{u_1u_2 + v_1v_2 - \frac{1}{2}\left(u_1v_2 + v_1u_2\right) + \frac{c^2}{a^2}w_1w_2}{\left\{\left(u_1^{\,2} + v_1^{\,2} - u_1v_1 + \frac{c^2}{a^2}w_1^{\,2}\right)\left(u_2^{\,2} + v_2^{\,2} - u_2v_2 + \frac{c^2}{a^2}w_2^{\,2}\right)\right\}^{\frac{1}{2}}} \tag{4}$$

It is clear in Figure 2.5 that the $(\bar{1}\,1\,0\,0)$, $(1\,1\,\bar{2}\,4)$, $(1\,1\,\bar{2}\,1)$ *et al.* poles of the C14 precipitate would exactly or nearly coincide with the $(\bar{1}\,1\,0)$, $(0\,0\,1)$, $(1\,1\,2)$ *et al.* poles of the matrix. These results are quite consistent with the observations of SADPs in Figures 2.3 and 2.4. On the basis of the preceding analyses, the orientation relationship between the C14 precipitate and A2 matrix can be best stated as follows:

$$(0\,0\,0\,1)_{C14}//(\bar{1}\,\bar{1}\,2)_m,\ (\bar{1}\,1\,0\,0)_{C14}//(\bar{1}\,1\,0)_m,\ (1\,1\,\bar{2}\,0)_{C14}//(1\,1\,1)_m.$$

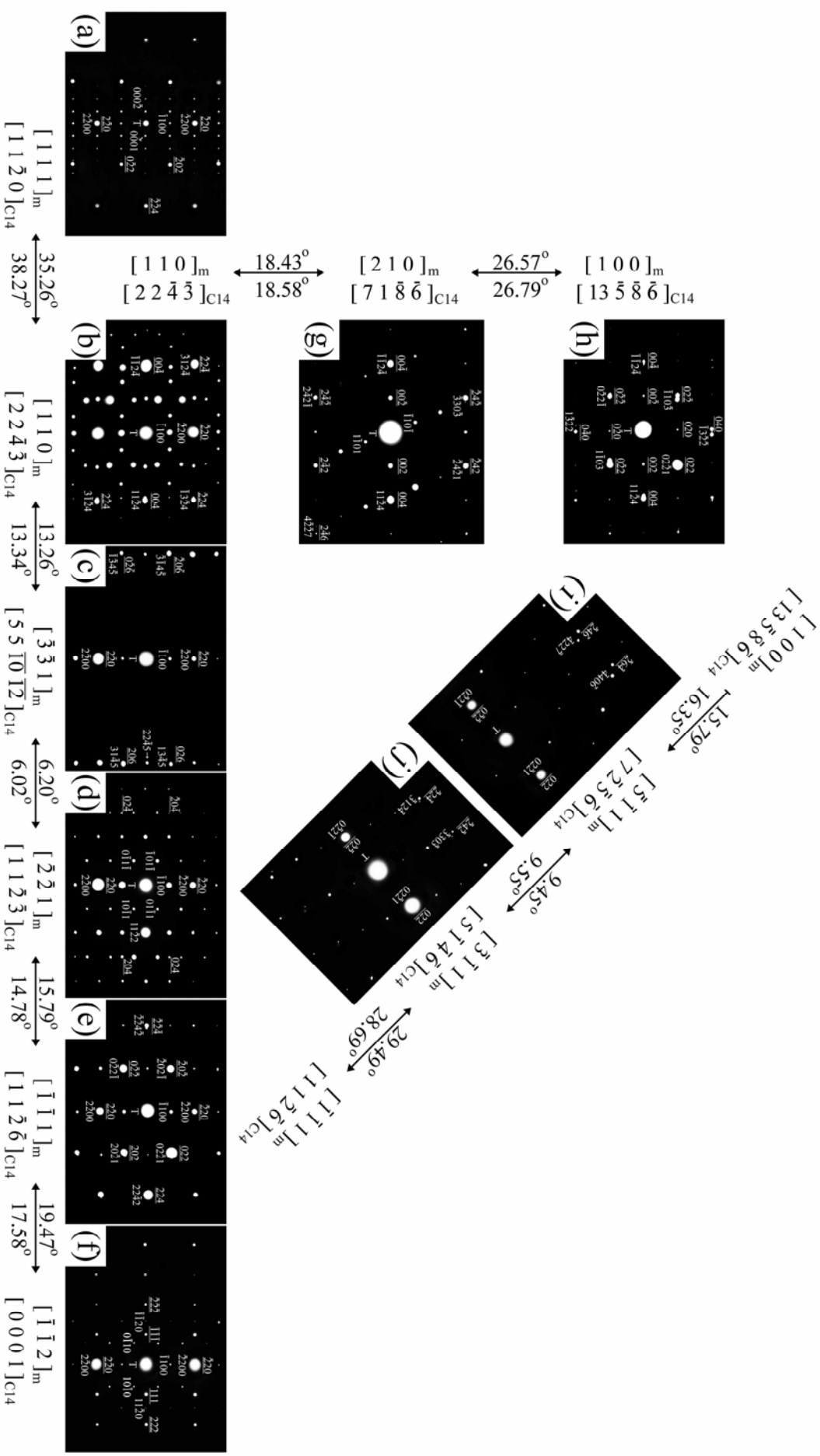
(a)
(b)
(c)
(d)
(e)
(f)
(g)
(h)
(i)
(j)
[1 1 1]m
[1 1 2̄ 0]C14
35.26°
38.27°
[1 1 0]m
[2 2 4̄ 3̄]C14
18.43°
18.58°
[2 1 0]m
[7 1 8̄ 6̄]C14
26.57°
26.79°
[1 0 0]m
[13 5̄ 8̄ 6̄]C14
[1 1 0]m
[2 2 4̄ 3̄]C14
13.26°
13.34°
[3̄ 3 1]m
[5 5 10̄ 12̄]C14
6.20°
6.02°
[2̄ 2̄ 1]m
[1 1 2̄ 3̄]C14
15.79°
14.78°
[1̄ 1̄ 1]m
[1 1 2̄ 6̄]C14
19.47°
17.58°
[1̄ 1̄ 2]m
[0 0 0 1]C14
[1 0 0]m
[13 5̄ 8̄ 6̄]C14
15.79°
16.35°
[5̄ 1 1]m
[7 2̄ 5̄ 6]C14
9.45°
9.55°
[3̄ 1 1]m
[5 1̄ 4̄ 6]C14
29.49°
28.69°
[1̄ 1̄ 1]m
[1 1 2̄ 6]C14

Figure 2.3 Ten SADPs taken from an area including the precipitate marked as “C” in Figure 2(a) and its surrounding matrix. The zone axes of the matrix are (a) $[1\ 1\ 1]$, (b) $[1\ 1\ 0]$, (c) $[\bar{3}\ \bar{3}\ 1]$, (d) $[\bar{2}\ \bar{2}\ 1]$, (e) $[\bar{1}\ \bar{1}\ 1]$, (f) $[\bar{1}\ \bar{1}\ 2]$, (g) $[2\ 1\ 0]$, (h) $[1\ 0\ 0]$, (i) $[\bar{5}\ \bar{1}\ 1]$ and (j) $[\bar{3}\ \bar{1}\ 1]$, respectively (hkil = C14 precipitate; hkl = matrix).

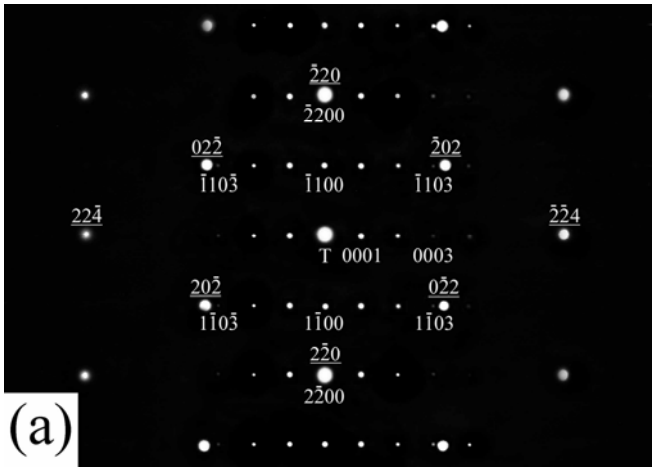

Figure 2.4 (a)

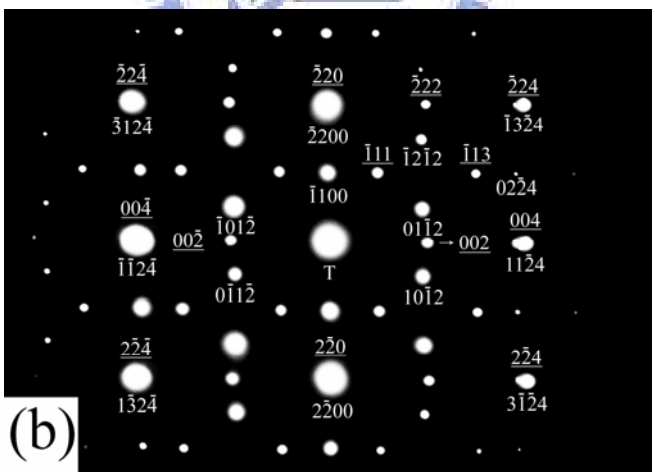

Figure 2.4 (b)

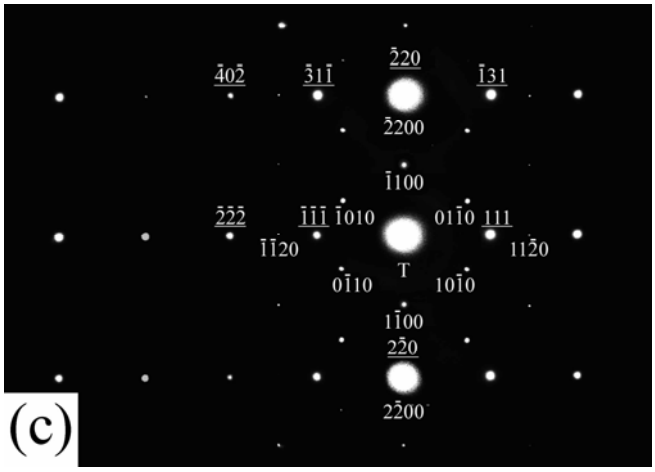

Figure 2.4 (c)

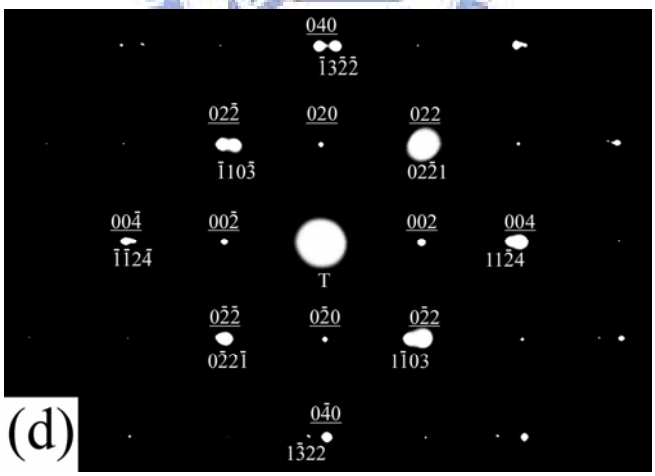

Figure 2.4 (d)

Figure 2.4 (a) through (d), higher magnification of Figures 2.3 (a), (b), (f) and (h), respectively (hkil = C14 precipitate; hkl = matrix).

Table 2.1 The d-spacings of the C14 phase

	Observed d-spacing*(nm)	Calculated d-spacing**(nm)	Indexed Plane
1	0.801	0.801	0001
2	0.437	0.437	$10\bar{1}0, 01\bar{1}0, 1\bar{1}00$
3	0.385	0.384	$10\bar{1}1, 10\bar{1}\bar{1}, 01\bar{1}1, 01\bar{1}\bar{1}, 1\bar{1}01, 1\bar{1}0\bar{1}$
4	0.294	0.295	$10\bar{1}2, 10\bar{1}\bar{2}, 01\bar{1}2, 01\bar{1}\bar{2}, 1\bar{1}02, 1\bar{1}0\bar{2}$
5	0.254	0.253	$11\bar{2}0, 1\bar{2}10, 2\bar{1}\bar{1}0$
6	0.240	0.241	$11\bar{2}1, 11\bar{2}\bar{1}, 1\bar{2}11, 1\bar{2}1\bar{1}, 2\bar{1}\bar{1}1, 2\bar{1}\bar{1}\bar{1}$
7	0.227	0.228	$10\bar{1}3, 10\bar{1}\bar{3}, 01\bar{1}3, 01\bar{1}\bar{3}, 1\bar{1}03, 1\bar{1}0\bar{3}$
8	0.214	0.214	$11\bar{2}2, 11\bar{2}\bar{2}, 1\bar{2}12, 1\bar{2}1\bar{2}, 2\bar{1}\bar{1}2, 2\bar{1}\bar{1}\bar{2}$
9	0.211	0.211	$20\bar{2}1, 20\bar{2}\bar{1}, 02\bar{2}1, 02\bar{2}\bar{1}, 2\bar{2}01, 2\bar{2}0\bar{1}$
10	0.183	0.183	$11\bar{2}3, 11\bar{2}\bar{3}, 1\bar{2}13, 1\bar{2}1\bar{3}, 2\bar{1}\bar{1}3, 2\bar{1}\bar{1}\bar{3}$
11	0.180	0.182	$10\bar{1}4, 10\bar{1}\bar{4}, 01\bar{1}4, 01\bar{1}\bar{4}, 1\bar{1}04, 1\bar{1}0\bar{4}$
12	0.168	0.169	$20\bar{2}3, 20\bar{2}\bar{3}, 02\bar{2}3, 02\bar{2}\bar{3}, 2\bar{2}03, 2\bar{2}0\bar{3}$
13	0.165	0.165	$12\bar{3}0, 21\bar{3}0, 1\bar{3}20, 3\bar{1}\bar{2}0, 2\bar{3}10, 3\bar{2}\bar{1}0$
14	0.157	0.159	$11\bar{2}4, 11\bar{2}\bar{4}, 1\bar{2}14, 1\bar{2}1\bar{4}, 2\bar{1}\bar{1}4, 2\bar{1}\bar{1}\bar{4}$

*The observed d-spacings were measured from SADPs.

**The calculated d-spacings were obtained on the basis of the hexagonal closed-packed structure with lattice parameters a = 0.505 nm, c = 0.801nm.

Table 2.2 Angles among some reciprocal vectors of matrix and C14 phase

	Two Desired Reciprocal Vectors	Observed Angle(Deg)	Calculated Angle(Deg)
Fig 2.3 (a)	$(\bar{1}\,\bar{1}\,2)_m$ and $(\bar{1}\,1\,0)_m$	90.0	90.0
	$(0\,0\,0\,1)_{C14}$ and $(\bar{1}\,1\,0\,0)_{C14}$	90.0	90.0
	$(\bar{1}\,1\,0)_m$ and $(\bar{1}\,0\,1)_m$	60.0	60.0
	$(\bar{1}\,1\,0\,0)_{C14}$ and $(\bar{1}\,1\,0\,3)_{C14}$	58.5	58.6
	$(\bar{1}\,0\,1)_m$ and $(\bar{1}\,\bar{1}\,2)_m$	30.0	30.0
	$(\bar{1}\,1\,0\,3)_{C14}$ and $(0\,0\,0\,1)_{C14}$	31.5	31.4
Fig 2.3 (b)	$(0\,0\,1)_m$ and $(\bar{1}\,1\,2)_m$	35.3	35.3
	$(1\,1\,\bar{2}\,4)_{C14}$ and $(\bar{1}\,3\,\bar{2}\,4)_{C14}$	35.5	35.6
	$(\bar{1}\,1\,2)_m$ and $(\bar{1}\,1\,0)_m$	54.7	54.7
	$(\bar{1}\,3\,\bar{2}\,4)_{C14}$ and $(\bar{1}\,1\,0\,0)_{C14}$	54.3	54.3
	$(\bar{1}\,1\,0)_m$ and $(0\,0\,1)_m$	90.0	90.0
	$(\bar{1}\,1\,0\,0)_{C14}$ and $(1\,1\,\bar{2}\,4)_{C14}$	90.0	90.0
Fig 2.3 (c)	$(1\,1\,6)_m$ and $(\bar{1}\,1\,0)_m$	90.0	90.00
	$(2\,2\,\bar{4}\,5)_{C14}$ and $(\bar{1}\,1\,0\,0)_{C14}$	90.0	90.00
	$(1\,1\,6)_m$ and $(0\,2\,6)_m$	12.9	12.9
	$(2\,2\,\bar{4}\,5)_{C14}$ and $(1\,3\,\bar{4}\,5)_{C14}$	12.9	12.8

	$(0\ 2\ 6)_m$ and $(\bar{1}\ 1\ 0)_m$	77.1	77.1
	$(1\ 3\ \bar{4}\ 5)_{C14}$ and $(\bar{1}\ 1\ 0\ 0)_{C14}$	77.1	77.2
Fig 2.3 (d)	$(1\ 1\ 4)_m$ and $(\bar{1}\ 1\ 0)_m$	90.0	90.0
	$(1\ 1\ \bar{2}\ 2)_{C14}$ and $(\bar{1}\ 1\ 0\ 0)_{C14}$	90.0	90.0
Fig 2.3 (e)	$(1\ 1\ 2)_m$ and $(\bar{1}\ 1\ 0)_m$	90.0	90.0
	$(1\ 1\ \bar{2}\ 1)_{C14}$ and $(\bar{1}\ 1\ 0\ 0)_{C14}$	90.0	90.0
	$(1\ 1\ 2)_m$ and $(0\ 1\ 1)_m$	30.0	30.0
	$(1\ 1\ \bar{2}\ 1)_{C14}$ and $(0\ 2\ \bar{2}\ 1)_{C14}$	29.0	28.8
	$(0\ 1\ 1)_m$ and $(\bar{1}\ 1\ 0)_m$	60.0	60.0
	$(0\ 2\ \bar{2}\ 1)_{C14}$ and $(\bar{1}\ 1\ 0\ 0)_{C14}$	61.0	61.2
Fig 2.3 (f)	$(1\ 1\ 1)_m$ and $(\bar{1}\ 1\ 0)_m$	90.0	90.0
	$(1\ 1\ \bar{2}\ 0)_{C14}$ and $(\bar{1}\ 1\ 0\ 0)_{C14}$	90.0	90.0
Fig 2.3 (g)	$(0\ 0\ 1)_m$ and $(\bar{1}\ 2\ 1)_m$	65.9	65.9
	$(1\ 1\ \bar{2}\ 4)_{C14}$ and $(\bar{2}\ 4\ \bar{2}\ 1)_{C14}$	64.5	64.6
	$(\bar{1}\ 2\ 1)_m$ and $(\bar{1}\ 2\ \bar{1})_m$	48.2	48.2
	$(\bar{2}\ 4\ \bar{2}\ 1)_{C14}$ and $(\bar{1}\ 1\ 0\ \bar{1})_{C14}$	47.5	47.5
	$(\bar{1}\ 2\ \bar{1})_m$ and $(0\ 0\ \bar{1})_m$	65.9	65.9
	$(\bar{1}\ 1\ 0\ \bar{1})_{C14}$and $(1\ 1\ \bar{2}\ 4)_{C14}$	69.0	68.77
Fig 2.3 (h)	$(0\ 0\ 1)_m$ and $(0\ 1\ 0)_m$	90.0	90.0
	$(1\ 1\ \bar{2}\ 4)_{C14}$ and $(\bar{1}\ 3\ \bar{2}\ \bar{2})_{C14}$	85.5	85.6

	$(0\ 0\ 1)_m$ and $(0\ 1\ 1)_m$	45.0	45.0
	$(1\ 1\ \bar{2}\ 4)_{C14}$ and $(0\ 2\ \bar{2}\ 1)_{C14}$	43.5	43.5
	$(0\ 0\ 1)_m$ and $(0\ \bar{1}\ 1)_m$	45.0	45.0
	$(1\ 1\ \bar{2}\ 4)_{C14}$ and $(1\ \bar{1}\ 0\ 3)_{C14}$	48.0	48.0
Fig 2.3 (i)	$(0\ 1\ 1)_m$ and $(\bar{1}\ 3\ \bar{2})_m$	79.1	79.1
	$(0\ 2\ \bar{2}\ 1)_{C14}$ and $(\bar{2}\ 2\ 0\ \bar{3})_{C14}$	78.0	78.1
	$(\bar{1}\ 3\ \bar{2})_m$ and $(\bar{1}\ 2\ \bar{3})_m$	21.8	21.8
	$(\bar{2}\ 2\ 0\ \bar{3})_{C14}$ and $(\bar{2}\ \bar{2}\ 4\ \bar{7})_{C14}$	23.2	23.2
Fig 2.3 (j)	$(0\ 1\ 1)_m$ and $(\bar{1}\ 2\ \bar{1})_m$	73.2	73.2
	$(0\ 2\ \bar{2}\ 1)_{C14}$ and $(\bar{1}\ 1\ 0\ \bar{1})_{C14}$	72.5	72.7
	$(\bar{1}\ 2\ \bar{1})_m$ and $(\bar{1}\ 1\ \bar{2})_m$	33.6	33.6
	$(\bar{1}\ 1\ 0\ \bar{1})_{C14}$ and $(\bar{3}\ 1\ 2\ \bar{4})_{C14}$	35.1	35.2

*The observed angles were measured from SADPs.

**The calculated angles were obtained on the basis of the hexagonal closed-packed structure with lattice parameters a = 0.505 nm, c = 0.801nm.

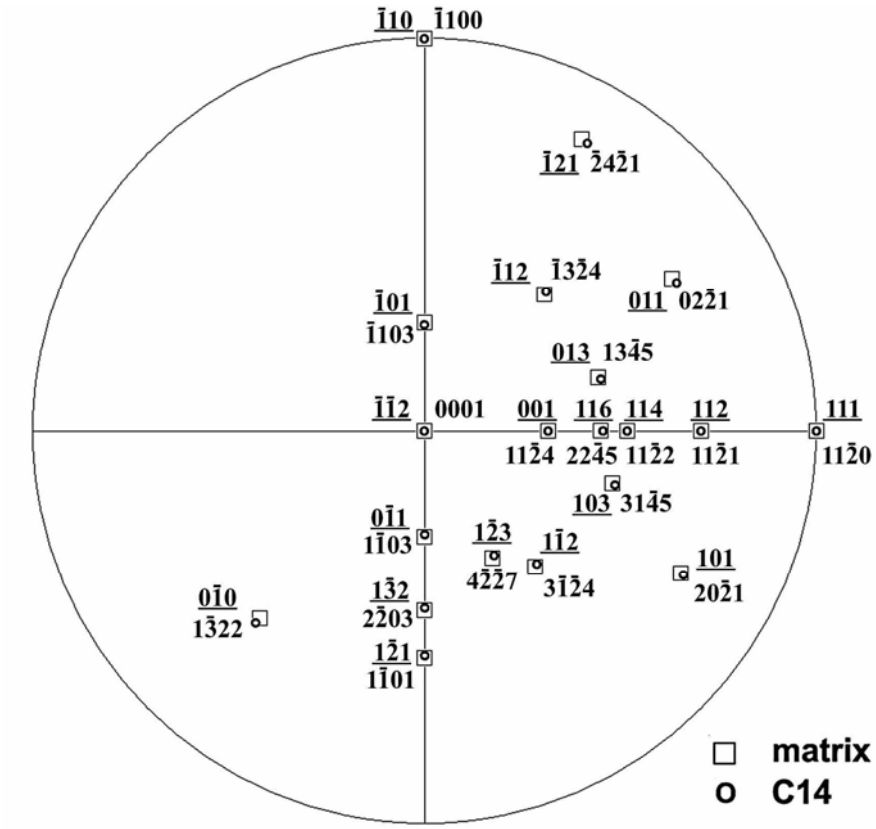

Figure 2.5 The superimposed C14/ferrite stereogram describing the orientation relationship between the C14 precipitate and ferrite matrix.

Table 2.3 Angle between two directions of matrix and C14 phase

Matrix	Calculated Angle(Deg)	C14	Calculated Angle(Deg)*
$[1\ 1\ 1]_m$ and $[1\ 1\ 0]_m$	35.26	$[1\ 1\ \bar{2}\ 0]_{C14}$ and $[2\ 2\ \bar{4}\ \bar{3}]_{C14}$	38.27
$[1\ 1\ 0]_m$ and $[\bar{3}\ \bar{3}\ 1]_m$	13.26	$[2\ 2\ \bar{4}\ \bar{3}]_{C14}$ and $[5\ 5\ \overline{10}\ \overline{12}]_{C14}$	13.34
$[\bar{3}\ \bar{3}\ 1]_m$ and $[\bar{2}\ \bar{2}\ 1]_m$	6.20	$[5\ 5\ \overline{10}\ \overline{12}]_{C14}$ and $[1\ 1\ \bar{2}\ \bar{3}]_{C14}$	6.02
$[\bar{2}\ \bar{2}\ 1]_m$ and $[\bar{1}\ \bar{1}\ 1]_m$	15.79	$[1\ 1\ \bar{2}\ \bar{3}]_{C14}$ and $[1\ 1\ \bar{2}\ \bar{6}]_{C14}$	14.78
$[\bar{1}\ \bar{1}\ 1]_m$ and $[\bar{1}\ \bar{1}\ 2]_m$	19.47	$[1\ 1\ \bar{2}\ \bar{6}]_{C14}$ and $[0\ 0\ 0\ 1]_{C14}$	17.58
$[1\ 1\ 0]_m$ and $[2\ 1\ 0]_m$	18.43	$[2\ 2\ \bar{4}\ \bar{3}]_{C14}$ and $[7\ 1\ \bar{8}\ \bar{6}]_{C14}$	18.58
$[2\ 1\ 0]_m$ and $[1\ 0\ 0]_m$	26.57	$[7\ 1\ \bar{8}\ \bar{6}]_{C14}$ and $[13\ \bar{5}\ \bar{8}\ \bar{6}]_{C14}$	26.79
$[1\ 0\ 0]_m$ and $[\bar{5}\ \bar{1}\ 1]_m$	15.79	$[13\ \bar{5}\ \bar{8}\ \bar{6}]_{C14}$ and $[7\ \bar{2}\ \bar{5}\ \bar{6}]_{C14}$	16.35
$[\bar{5}\ \bar{1}\ 1]_m$ and $[\bar{3}\ \bar{1}\ 1]_m$	9.45	$[7\ \bar{2}\ \bar{5}\ \bar{6}]_{C14}$ and $[5\ \bar{1}\ \bar{4}\ \bar{6}]_{C14}$	9.55
$[\bar{3}\ \bar{1}\ 1]_m$ and $[\bar{1}\ \bar{1}\ 1]_m$	29.49	$[5\ \bar{1}\ \bar{4}\ \bar{6}]_{C14}$ and $[1\ 1\ \bar{2}\ \bar{6}]_{C14}$	28.69

*The calculated angles were obtained on the basis of the hexagonal closed-packed structure with lattice parameters a = 0.505nm, c = 0.801nm.

Finally, it is worthwhile to mention that the C14 precipitate was also observed by many workers in Fe-Al-Nb, Fe-Al-Zr and Fe-Al-Ta alloys [4, 9-10]. However, we are aware of only one article, in which the orientation relationship between the C14 precipitate and A2 matrix was predicted. In 2005, Morris et al. reported that when the Fe-25Al-2Nb alloy was aged at 800˚C or 900˚C, C14 precipitate were formed within the A2 matrix; the orientation relationship between the C14 precipitate and A2 matrix was $\{\bar{1}\,0\,1\,0\}_{C14}//\{\bar{1}\,0\,1\}_m$, $<1\,\bar{2}\,1\,0>_{C14} \approx <0\,1\,0>_m$ and $<0\,0\,0\,1>_{C14} \approx <1\,0\,1>_m$, which was determined by using two SADPs [9]. In the previous study, it is found that their two SADPs were taken far away from the exact zone axes and $(1\,0\,\bar{1}\,0)_{C14}$ reflection spot was nearly parallel to the $(\bar{1}\,0\,1)_m$ reflection spot. Accordingly, Morris *et al.* claimed that the only exact relationship was $\{\bar{1}\,0\,1\,0\}_{C14}//\{\bar{1}\,0\,1\}_m$ and all other relationships were approximate with a difference of a few degrees (3~5˚) [9]. Interestingly, it is noted here that the previous result of $\{\bar{1}\,0\,1\,0\}_{C14}//\{\bar{1}\,0\,1\}_m$ is indeed in agreement with that observed in Figure 2.4(c) of the present work.

2-4 Conclusions

The orientation relationship between C14 precipitate and ferrite matrix in an Fe-20 at.% Al-8 at.% Ti alloy has been studied by using transmission electron microscopy.

1. In the as-quenched condition, the microstructure of the Fe-20 at.% Al-8 at.% Ti alloy was a mixture of (A2+$D0_3$) phases which was formed by an A2→B2→(A2+$D0_3$) ordering transitions during quenching.
2. When the alloy was aged at 1000˚C, a kind of plate-like precipitate was formed within the A2 matrix. The plate-like precipitate has a hexagonal C14 structure with *a* = 0.505 nm and *c* = 0.801 nm.
3. The orientation relationship between the C14 precipitate and A2 matrix was determined to be $(0001)_{C14}//(\bar{1}\bar{1}2)_m$, $(\bar{1}100)_{C14}//(\bar{1}10)_m$, $(11\bar{2}0)_{C14}//(111)_m$ which has never been reported in the Fe-Al-Ti alloys system.

.

References

1. M.G. Mediratta, S.K. Ehlers, H.A. Lipsitt, Metall. Trans. A 18 (1987) 509.
2. C.H. Sellers, T.A. Hyde, T.K. O'Brien, R.N. Wright, J. Phys. Chem. Solids 55 (1994) 505.
3. U. Prakash, G. Sauthoff, Intermetallics 9 (2001) 107.
4. M. Palm, Intermetallics 13 (2005) 1286.
5. M. Palm, G. Sauthoff, Intermetallics 12 (2004) 1345.
6. M. Palm, G. Inden, N. Thomas, J. Phase Equilibria 16 (1995) 209.
7. C.H. Chen, T.F. Liu, Metall. Trans. A 34 (2003) 503.
8. J. W. Edington, The Operation and Calibration of the Electron Microscope, Vol.1, (1985).
9. D.G. Morris, L.M. Requejo, M.A. Muñoz-Morris, Intermetallics 13 (2005) 862.
10. F. Stein, M. Palm, G. Sauthoff, Intermetallics 13 (2005) 1056.
11. F. Stein, M. Palm, G. Sauthoff, Intermetallics 13 (2005) 1275.

Chapter 3.

Formation of (B2+$D0_3$) phases at a/2<100> anti-phase boundary in an Fe-23 at.% Al-8.5 at.% Ti alloy

Formation of (B2+$D0_3$) phases at a/2<100> anti-phase boundary in an Fe-23 at.% Al-8.5 at.% Ti alloy

Abstract

The as-quenched microstructure of the Fe-23 at.% Al-8.5 at.% Ti alloy was a mixture of (A2+$D0_3$) phases. Transmission electron microscopy (TEM) examinations indicated that when the alloy was aged at 900˚C, the size of the $D0_3$ domains increased with increasing the aging time, and an A2 → (A2+$D0_3$) → (B2+$D0_3$) transition occurred at a/2<100> anti-phase boundaries (APBs). This feature has never been reported by other workers in the Fe-Al-Ti alloy systems before.

3-1 Introduction

In order to improve high temperature oxidation and mechanical properties, Ti has been added to the Fe-Al binary alloys [1-5]. Based on these results, it can be generally concluded that the addition of Ti can effectively improve these properties. In addition, the effects of Ti addition on the microstructures of the Fe-Al binary alloys have also been studied by many workers [3-13]. It was reported that the addition of Ti would strongly increase the $D0_3 \rightarrow B2$ and $B2 \rightarrow A2$ transition temperatures [6-13], and expand the $(A2+D0_3)$ phase field [10-12]. Furthermore, a $(B2+D0_3)$ two-phase field was claimed to be existent in the Fe-Al-Ti ternary alloys [11-13]. It is worthwhile to note that the $(B2+D0_3)$ two-phase field has not been found by previous workers in the Fe-Al binary alloys before [14-16]. However, to date, the existence of the $(B2+D0_3)$ two-phase field in the Fe-Al-Ti ternary alloys was confirmed principally by using X-ray diffraction and electron-probe microanalysis [11-13]. In order to clarify the microstructural revolution for the formation of the $(B2+D0_3)$ phases, an TEM study was performed to investigate the phase transition in the Fe-23 at.% Al-8.5 at.% Ti alloy.

3-2 Experimental procedure

The Fe-23 at.% Al-8.5 at.% Ti alloy was prepared in a vacuum induction furnace by using pure Fe (99.9%), Al (99.9%) and Ti (99.9%). After being homogenized at 1250˚C for 48 h, the ingot was sectioned into 2-mm-thick slices. These slices were subsequently solution heat-treated at 1100˚C for 1 h and then quenched into room-temperature water rapidly. The aging processes were performed at 900˚C for various times in a vacuum heat-treated furnace and then quenched rapidly. TEM specimens were prepared by double-jet electropolisher with an electrolyte of 67% methanol and 33% nitric acid. Electron microscopy was performed on a JEOL JEM-2000FX TEM operating at 200kV. Elemental concentrations were examined by using a Link ISIS 300 energy-dispersive X-ray spectrometer (EDS). Quantitative analyses of elemental concentrations for Fe, Al and Ti were made with a Cliff-Lorimer Ratio Thin Section method.

3-3 Results and discussion

Figure 3.1(a) shows a selected-area diffraction pattern of the as-quenched alloy, revealing the presence of the superlattice reflection spots of the ordered $D0_3$ phase [17]. Figures 3.1(b) and (c) are (111) $D0_3$ and (200) $D0_3$ (or, equivalently, (100) B2) dark-field (DF) electron micrographs of the as-quenched alloy, exhibiting the presence of fine $D0_3$ domains with a/2<100> APBs and small B2 domains with a/4<111> APBs, respectively [15,16]. In Figure 3.1(c), it is also seen that a high density of disordered A2 phase showing a dark contrast could be observed within the B2 domains. Accordingly, the as-quenched microstructure of the alloy was a mixture of (A2+$D0_3$) phases. This is similar to that reported by other workers in the as-quenched Fe-(18~22.5) at.% Al-5 at.% Ti alloys [10].

When the as-quenched alloy was aged at 900˚C for a short time, the $D0_3$ domains grew with preferred orientation, as shown in Figure 3.2. This feature is similar to that reported by other workers in the aged Fe-Al-Ti alloys [10]. In Figure 3.2, it is also seen that the a/2<100> APBs were coated with a continuous layer of the disordered A2 phase. However, after prolonged aging at 900˚C, some fine particles started to appear within the A2 phase. Figures 3.3(a) and (b) are (111) and (200) $D0_3$ DF electron micrographs of the alloy aged at 900˚C for 1 h, clearly revealing that the

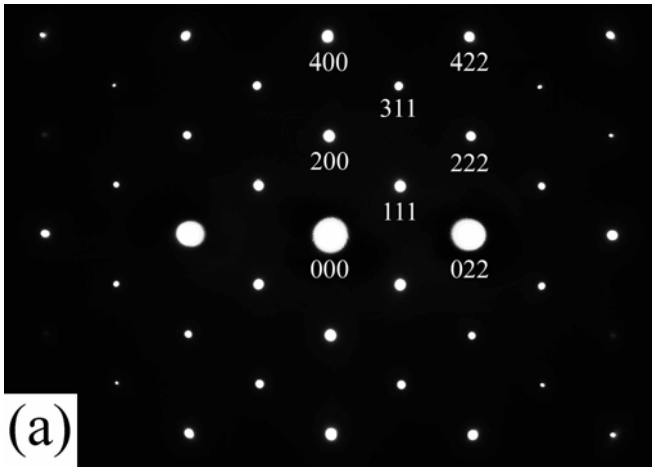

Figure 3.1 (a)

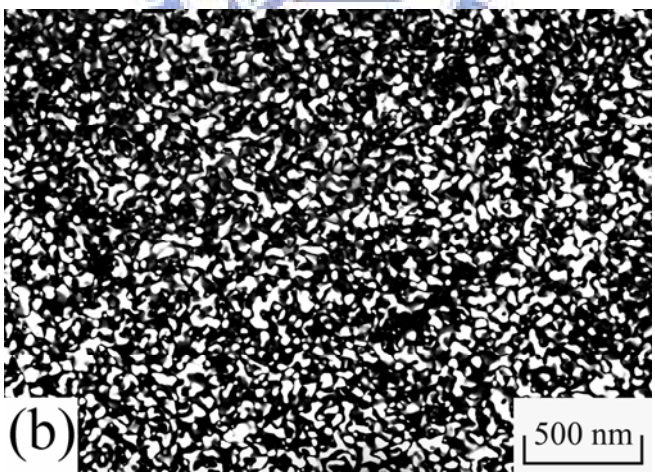

Figure 3.1 (b)

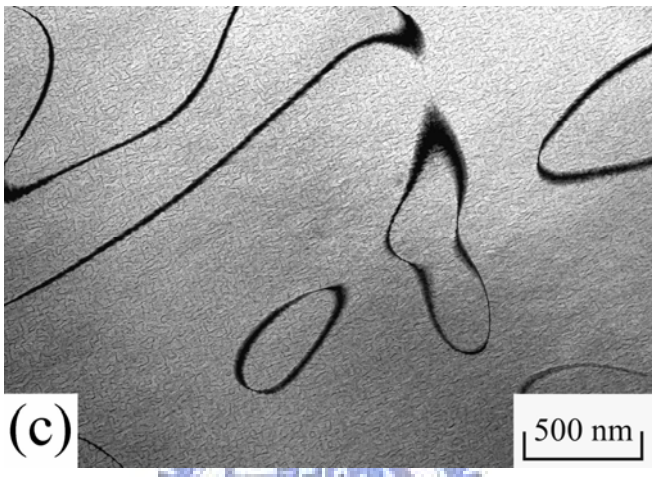

Figure 3.1 (c)

Figure 3.1 Electron micrographs of the as-quenched alloy: (a) a selected-area diffraction pattern. The foil normal is $[01\bar{1}]$. (hkl = $D0_3$ phase.), (b) and (c) (111) and (200) $D0_3$ DF, respectively.

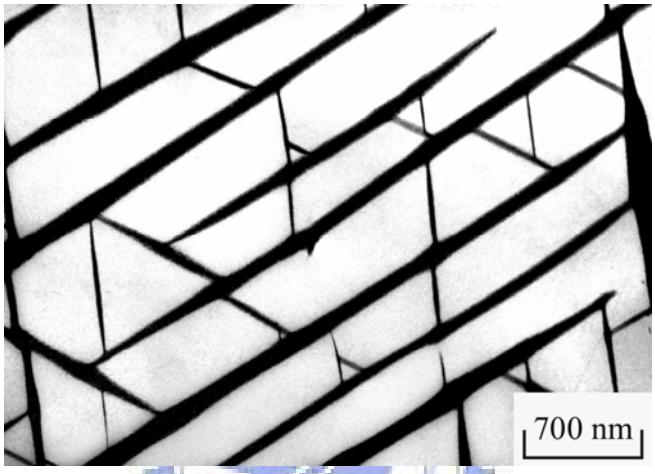

Figure 3.2 (200)$D0_3$ DF electron micrograph of the alloy aged at 900˚C for 0.5 h.

(111) $D0_3$ DF image and (200) $D0_3$ DF image are morphologically identical. Since the (200) reflection spot comes from both the B2 and $D0_3$ phases, while the (111) reflection spot comes only from $D0_3$ phase [10,12], the fine bright particles at a/2<100> APBs presented in Figures 3.3(a) and (b) are considered to be $D0_3$ phase. TEM examinations indicated that no evidence of the a/4<111> APBs could be observed. This result seems to imply that the B2 domains would grow up to the whole grains during aging. With increasing the aging time at 900˚C, the amount of the $D0_3$ particles at a/2<100> APBs increased and the disordered A2 phase decreased, as illustrated in Figure 3.4. By comparing Figures 3.3 and 3.4, it is also seen that the breadth of the a/2<100> APBs became broader as the aging time increased. TEM examinations of thin foils indicated that prolonged aging at the same temperature resulted in the broadening of the a/2<100> APBs to proceed, as shown in Figure 3.5. Figure 3.5(a), (111) $D0_3$ DF electron micrograph of the alloy aged at 900˚C for 24 h, indicates that at a/2<100> APBs, the amount of the $D0_3$ particles increased considerably and a dark contrast could also be detected between the particles. However, a (200) $D0_3$ DF electron micrograph (Figure 3.5(b)) reveals that the whole regions of the a/2<100> APBs were full bright in contrast. This indicates that the dark regions at a/2<100> APBs presented in Figure

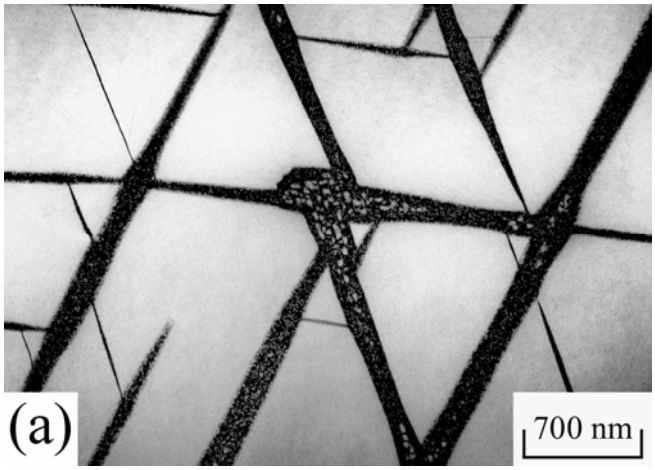

Figure 3.3 (a)

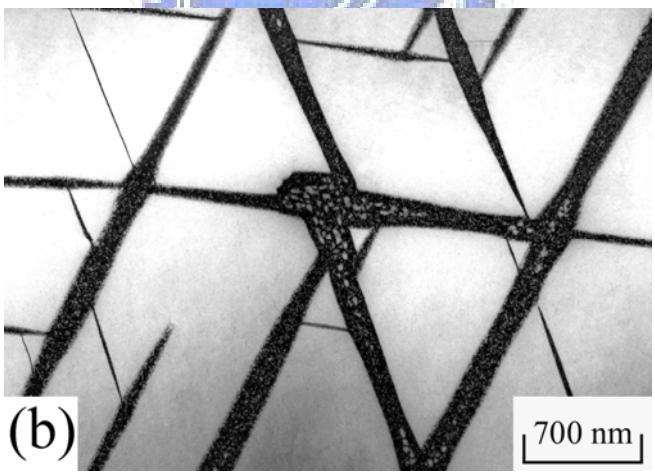

Figure 3.3 (b)

Figure 3.3 Electron micrographs of the alloy aged at 900˚C for 1 h. (a) and (b) (111) and (200) $D0_3$ DF, respectively.

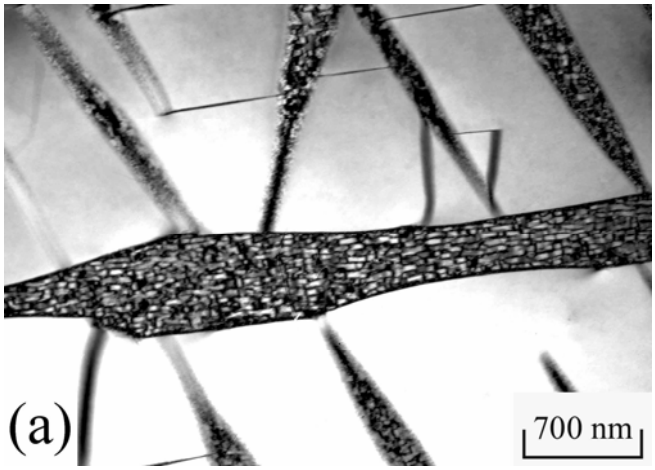

Figure 3.4 (a)

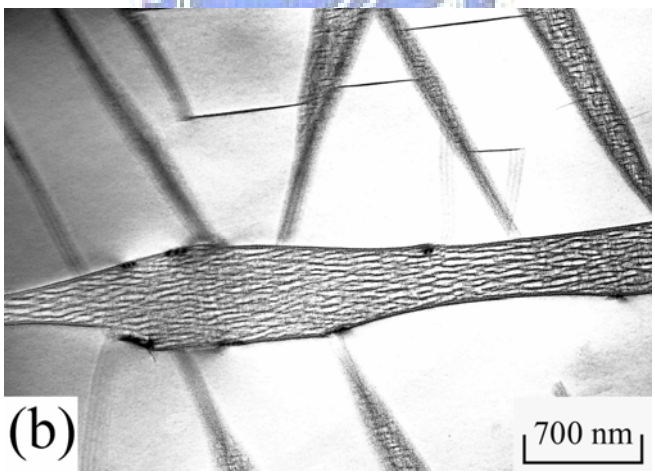

Figure 3.4 (b)

Figure 3.4 Electron micrographs of the alloy aged at 900˚C for 6 h. (a) and (b) (111) and (200) $D0_3$ DF, respectively.

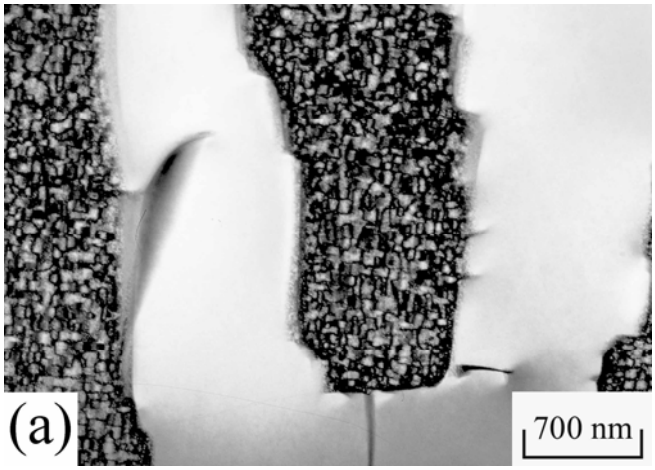

Figure 3.5 (a)

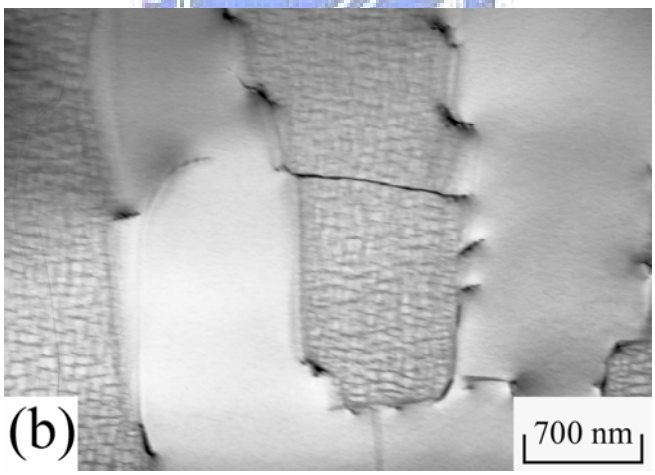

Figure 3.5 (b)

Figure 3.5 Electron micrographs of the alloy aged at 900˚C for 24 h. (a) and (b) (111) and (200) $D0_3$ DF, respectively.

3.5(a) should be of the B2 phase. Consequently, when the alloy was aged at 900˚C for longer times, the microstructure at the a/2<100> APBs was a mixture of (B2+$D0_3$) phases.

The fact that with increasing aging time at 900˚C the size of the $D0_3$ domains existing in the as-quenched alloy increased and an A2 → (A2+$D0_3$) → (B2+$D0_3$) transition occurred at a/2<100> APBs is a remarkable feature in the present study. This feature has never been reported by previous workers in the Fe-Al-Ti alloy systems before. In order to clarify this feature, the quantitatively EDS analyses were undertaken. The results are shown in Table 3.1. It is seen in Table 3.1 that when the alloy was aged at 900˚C for 0.5 h, the Al and Ti concentrations in the $D0_3$ domains were much greater than those in the as-quenched alloy, and these concentrations were noticeably lower at a/2<100> APBs. The insufficient concentrations of both Al and Ti would cause the disordered A2 phase to form at a/2<100> APBs. However, along with the growth of the $D0_3$ domains, partial Al and Ti atoms would proceed to diffuse toward the a/2<100> APBs. EDS analyses indicated that during the early stage of isothermal aging at 900˚C, the increased amount of Ti at a/2<100> APBs was more than that of Al. It implies that during aging, Ti redistributed first and then Al started to move appreciably. This result is

consistent with that found by other workers in the Fe-Al-Ti ternary alloys [18], in which they reported that the diffusion of Ti is faster than that of Al. Furthermore, it is well-known that a small amount of Ti addition in the Fe-Al binary alloys would strongly enhance the formation of the $D0_3$ phase [10-12]. Therefore, it is plausible to suggest that the drastic increase of Ti concentration should be favorable for the formation of the fine $D0_3$ particles at a/2<100> APBs, which is consistent with the observation in Figure 3.3. With increasing aging time at 900˚C, both Al and Ti concentrations at a/2<100> APBs continue to increase significantly. It is thus expected that owing to the increase of Al and Ti, the amount of the fine $D0_3$ particles at a/2<100> APBs would increase and the microstructure of the remaining regions would transform from the disordered A2 phase to B2 phase, as observed in Figures 3.4 and 3.5.

Finally, it is interesting to note that compared to the previously established isothermal sections of the Fe-Al-Ti ternary alloys at 900˚C, the chemical compositions of Fe-23.8 at.% Al-11.1 at.% Ti and Fe-22.4 at.% Al-7.4 at.% Ti obtained from the $D0_3$ domain and (B2+$D0_3$) region in the present alloy aged at 900˚C for 24 h are just located in the $D0_3$ and (B2+$D0_3$) regions, respectively [12].

Table 3.1 Chemical Compositions of the Phases Revealed by Energy-Dispersive X-ray Spectrometer (EDS)

Heat Treatment	Phase	Chemical Compositions (at.%)		
		Fe	Al	Ti
as-quenched	A2+$D0_3$	68.3	23.1	8.6
900°C, 0.5 h	$D0_3$ domain	62.5	25.1	12.4
	APB(A2)	75.9	19.8	4.3
900°C, 1 h	$D0_3$ domain	63.5	24.9	11.6
	APB(A2+$D0_3$)	73.6	20.2	6.2
900°C, 6 h	$D0_3$ domain	64.4	24.3	11.3
	APB(A2+B2+$D0_3$)	71.6	21.5	6.9
900°C, 24 h	$D0_3$ domain	65.1	23.8	11.1
	APB(B2+$D0_3$)	70.2	22.4	7.4

3-4 Conclusions

The phase transformations in an Fe-23 at.% Al-8.5 at.% Ti alloy have been studied by using transmission electron microscopy and energy-dispersive X-ray spectrometry.

1. In the as-quenched condition, the microstructure of the Fe-23 at.%Al-8.5 at.%Ti alloy was a mixture of (A2+$D0_3$) phases which was formed by an A2→B2→(A2+$D0_3$) ordering transitions during quenching.
2. When the alloy was aged at 900˚C, the $D0_3$ domains existing in the as-quenched alloy grew and an A2 → (A2+$D0_3$) → (B2+$D0_3$) transition occurred at a/2<100> APBs of the $D0_3$ domains. The microstructural revolution has never been reported by other workers in the Fe-Al-Ti alloy systems before.

References

1. F. Dobeš, P. Kratochvíl, K. Milička, Intermetallics 14 (2006) 1199.
2. S.M. Zhu, K. Sakamoto, M. Tamura, K. Iwasaki, Scripta Mater. 42 (2000) 905.
3. U. Prakash, G. Sauthoff, Intermetallics 9 (2001) 107.
4. M. Palm, G. Sauthoff, Intermetallics 12 (2004) 1345.
5. M. Palm, J. Lacaze, Intermetallics 14 (2006) 1291.
6. F. Stein, A. Schneider, G. Frommeyer, Intermetallics 11 (2003) 71.
7. L. Anthony, B. Fultz, Acta Metall. Mater. 43 (1995) 3885.
8. M. Palm, Intermetallics 13 (2005) 1286.
9. Y. Nishino, S. Asano, T. Ogawa, Mater. Sci. Eng. A 234-236 (1997) 271.
10. M.G. Mediratta, S.K. Ehlers, H.A. Lipsitt, Metall. Trans. A 18 (1987) 509.
11. G. Ghosh, in: G. Effenberg (Eds.), Ternary Alloy Systems, Springer Berlin Heidelberg, New York, 2005, pp. 426-452.
12. I. Ohnuma, C.G. Schön, R. Kainuma, G. Inden, K. Ishida, Acta Mater. 46 (1998) 2083.
13. S.M. Zhu, K. Sakamoto, M. Tamura, K. Iwasaki, Mater. Trans. JIM. 42 (2001) 484.

14. O. Ikeda, I. Ohnuma, R. Kainuma, K. Ishida, Intermetallics 9 (2001) 755.

15. S.M. Allen, J.W. Cahn, Acta Metall. 24 (1976) 425.

16. P.R. Swann, W.R. Duff, R.M. Fisher, Metall. Trans. 3 (1972) 409.

17. C.H. Chen, T.F. Liu, Metall. Trans. A 34 (2003) 503.

18. J. Ni, T. Ashino, S. Iwata, Acta Mater. 48 (2000) 3193.

Chapter 4.

Phase separation from $D0_3$ to ($B2+D0_3$) in an Fe-24.6 at.% Al-7.5 at.% Ti alloy

Phase separation from $D0_3$ to ($B2+D0_3$) in an Fe-24.6 at.% Al-7.5 at.% Ti alloy

Abstract

The as-quenched microstructure of the Fe-24.6 at.% Al-7.5 at.% Ti alloy was a mixture of ($A2+D0_3$) phases. When the alloy was aged at 900°C for moderate times, the $D0_3$ domains grew considerably and B2 phase appeared on a/2<100> anti-phase boundaries (APBs). With continued aging at 900°C, phase separation from prior-$D0_3$ to ($B2+D0_3$*) occurred initially on a/2<100> APBs, and then proceeded toward the whole prior-$D0_3$ domains. This microstructural revolution has never been reported by other workers in the Fe-Al-Ti alloy systems before.

4-1 Introduction

Effects of Ti addition on the microstructures of the Fe-Al binary alloys have been studied by many workers [1-8]. Based on these results, it can be generally concluded that the Ti addition in the Fe-Al binary alloys would (1) strongly increase the $D0_3 \rightarrow B2$ transition temperature [5-7], (2) significantly expand the ($A2+D0_3$) phase field [6-8], and (3) cause the $D0_3$ anti-phase boundaries (APBs) to exhibit a tendency toward anisotropy [5]. Furthermore, a ($B2+D0_3$) two-phase field was claimed to be existent at temperatures ranging from 800˚C to 1000˚C in the Fe-Al-Ti ternary alloys [6-8]. It is noted that the ($B2+D0_3$) two-phase field has not been found by previous workers in the Fe-Al binary alloys before [9-11]. However, up to now, the existence of the ($B2+D0_3$) two-phase field in the Fe-Al-Ti ternary alloys was confirmed principally by using X-ray diffraction and electron-probe microanalysis [6-8]. Little TEM information concerning the microstructural revolution for the formation of ($B2+D0_3$) phases has been provided. The present investigation, using TEM, is an attempt to clarify the microstructural revolution for the formation of ($B2+D0_3$) phases in the Fe-24.6 at.% Al-7.5 at.% Ti alloy after being aged at 900˚C. In the present study, the chemical compositions of the alloy were just located in the ($B2+D0_3$) phase-field in Fe-Al-Ti ternary phase diagram at 900˚C.

4-2 Experimental procedure

An ingot of the Fe-24.6 at.% Al-7.5 at.% Ti alloy was prepared in a vacuum induction furnace by using pure Fe(99.9%), Al(99.9%) and Ti(99.9%). After being homogenized at 1250˚C for 48 h, the ingot was sectioned into 2-mm-thick slices. These slices were subsequently solution heat-treated at 1100˚C for 1 h and then quenched into room-temperature water rapidly. The aging processes were performed at 900˚C for various times in a vacuum heat-treated furnace and then quenched rapidly. TEM specimens were prepared by means of double-jet electropolisher with an electrolyte of 67% methanol and 33% nitric acid. Electron microscopy was performed on a JEOL JEM-2000FX scanning transmission electron microscope operating at 200kV. This microscope was equipped with a Link ISIS 300 energy-dispersive X-ray spectrometer (EDS) for chemical analysis. Quantitative analyses of elemental concentrations for Fe, Al and Ti were made with the aid of a Cliff-Lorimer Ratio Thin Section method.

4-3 Results and discussion

Figure 4.1(a) is a selected-area diffraction pattern (SADP) of the as-quenched alloy, exhibiting the superlattice reflection spots of the ordered $D0_3$ phase [12,13]. Figures 4.1(b) and (c) are (200) $D0_3$ (or equivalently (100) B2) and $(\bar{1}11)$ $D0_3$ dark-field (DF) electron micrographs of the as-quenched alloy, showing the presence of the small B2 domains with a/4<111> APBs and fine $D0_3$ domains with a/2<100> APBs, respectively. In Figures 4.1(b) and (c), it is seen that the sizes of both B2 and $D0_3$ domains are very small, indicating that these domains were formed by ordering transition during quenching [11-16]. In Figure 4.1(b), it is also seen that a high density of disordered A2 phase (dark contrast) could be observed within the B2 domains. Accordingly, the as-quenched microstructure of the alloy was a mixture of (A2+$D0_3$) phases.

Figure 4.2(a) shows a $(\bar{1}11)$ $D0_3$ DF electron micrograph of alloy aged at 900˚C for 6 h, indicating that the $D0_3$ domains grew significantly. Figure 4.2(b), a (200) $D0_3$ DF electron micrograph of the same area as Figure 4.2(a), revealing that the disordered A2 phase wetted on the a/2<100> APBs; otherwise there would be no contrast from these boundaries using a (200) reflection [11]. With the subsequent aging at 900˚C, the disordered A2 phase disappeared and a phase separation started to

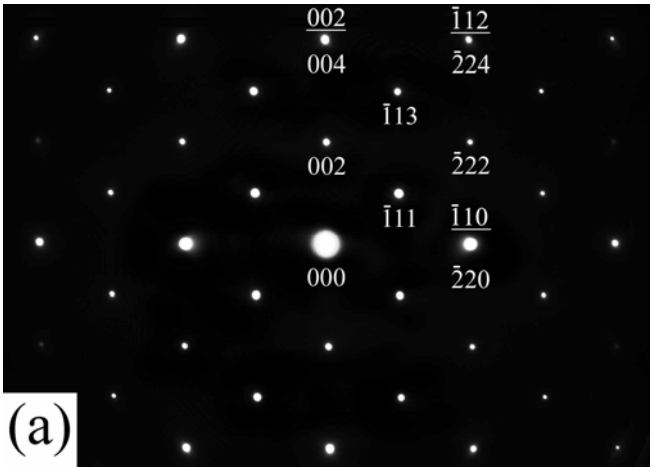

Figure 4.1 (a)

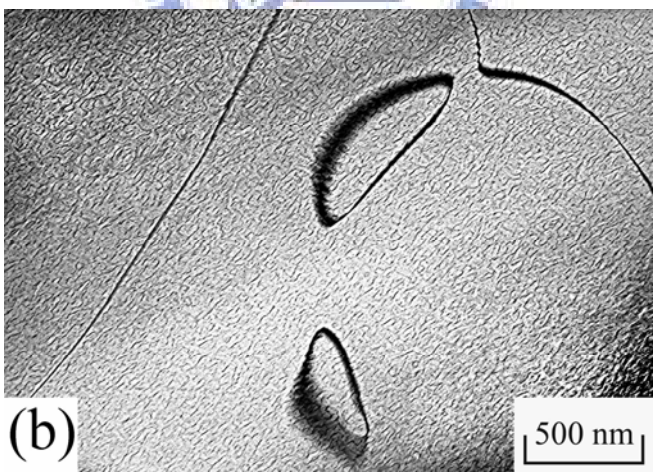

Figure 4.1 (b)

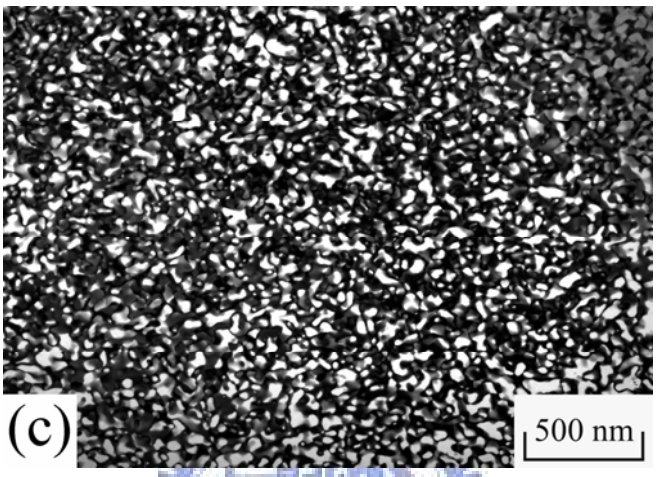

Figure 4.1 (c)

Figure 4.1 Electron micrographs of the as-quenched alloy: (a) a selected-area diffraction pattern. The foil normal is [110]. (hkl = $D0_3$ phase, <u>hkl</u> = A2 phase.), (b) and (c) (200) and ($\bar{1}11$) $D0_3$ DF, respectively.

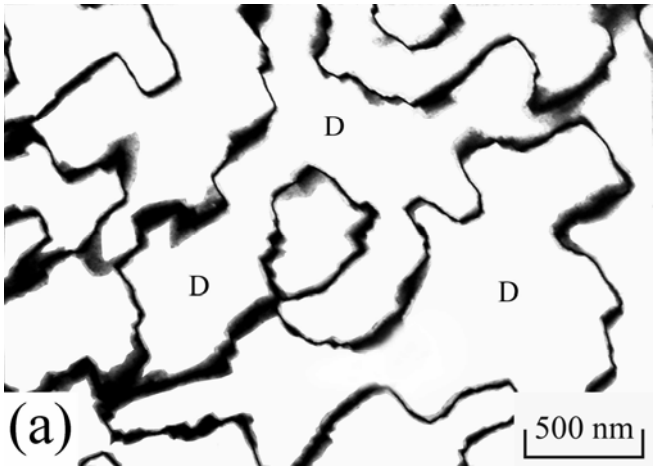

Figure 4.2 (a)

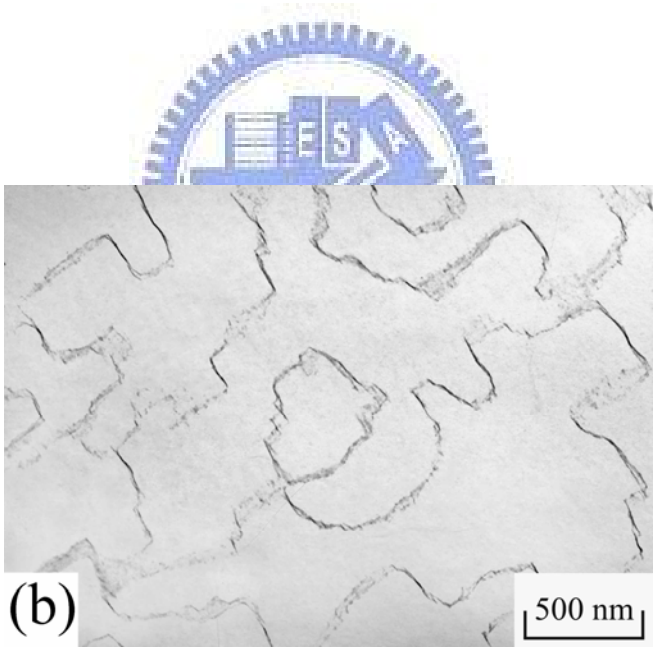

Figure 4.2 (b)

Figure 4.2 Electron micrographs of the alloy aged at 900˚C for 6 h. (a) and (b) ($\bar{1}11$) and (200) $D0_3$ DF, respectively.

occur basically at a/2<100> APBs of the $D0_3$ domains. A typical example is shown in Figure 4.3. Figure 4.3(a) is a $(\bar{1}11)$ $D0_3$ DF electron micrograph of the alloy aged at 900˚C for 24 h, revealing that the a/2<100> APBs broadened and the well-grown prior-$D0_3$ domains decomposed into small $D0_3$* domains (as indicated by the white arrow and designated as $D0_3$* domain to be distinguished from the original $D0_3$ domain) separated by dark layers. Shown in Figure 4.3(b) is a (200) $D0_3$ DF electron micrograph taken from the same area as Figure 4.3(a), clearly indicating that the whole region is bright in contrast. This demonstrates that these dark layers should be of B2 phase, rather than disordered A2 phase. Obviously, it is seen in Figure 4.3(a) that with increased aging time at 900˚C, B2 phase started to form at a/2<100> APBs and phase separation from $D0_3$ to (B2+$D0_3$*) occurred initially on a/2<100> APBs. Transmission electron microscopy examinations revealed that when the alloy was aged at 900˚C for longer times and then quenched, the phase separation from $D0_3$ to (B2+$D0_3$*) proceeded toward the whole prior-$D0_3$ domains. A typical example is illustrated in Figure 4.4. Therefore, it is thus anticipated that the microstructure of the alloy in the equilibrium stage at 900˚C should be a mixture of (B2+$D0_3$*) phases.

On the basis of preceding results, it is obvious that when the present

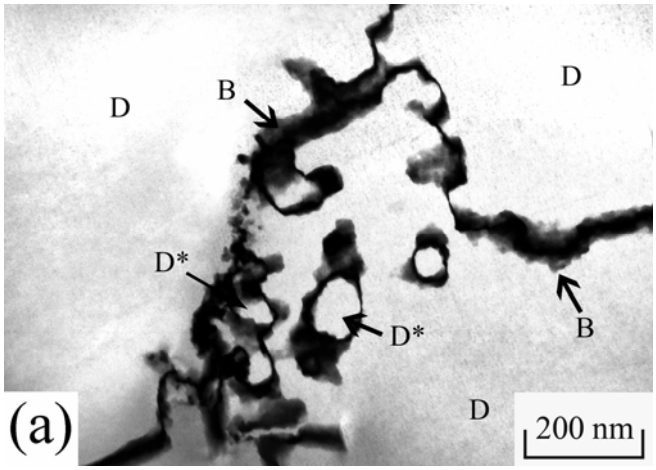

Figure 4.3 (a)

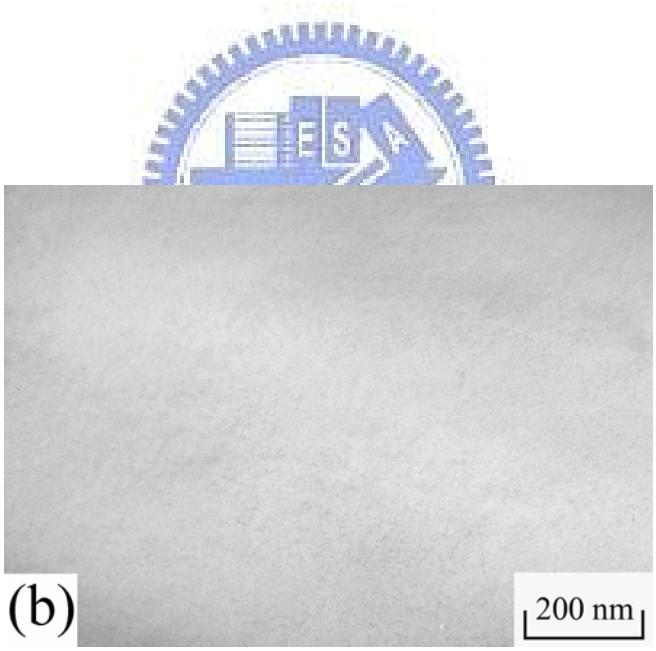

Figure 4.3 (b)

Figure 4.3 Electron micrographs of the alloy aged at 900˚C for 24 h. (a) and (b) ($\bar{1}11$) and (200) $D0_3$ DF, respectively.

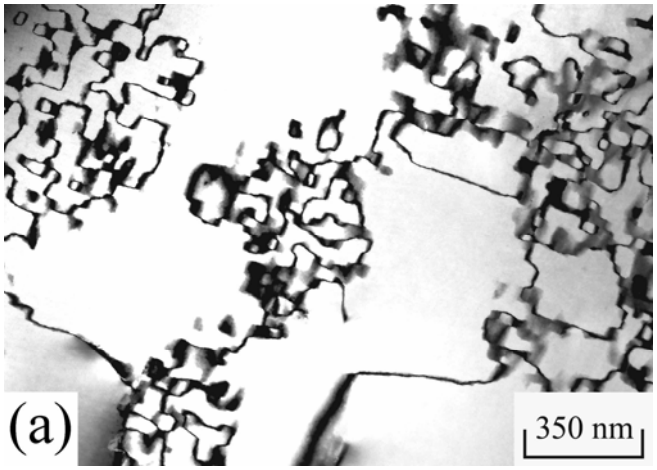

Figure 4.4 (a)

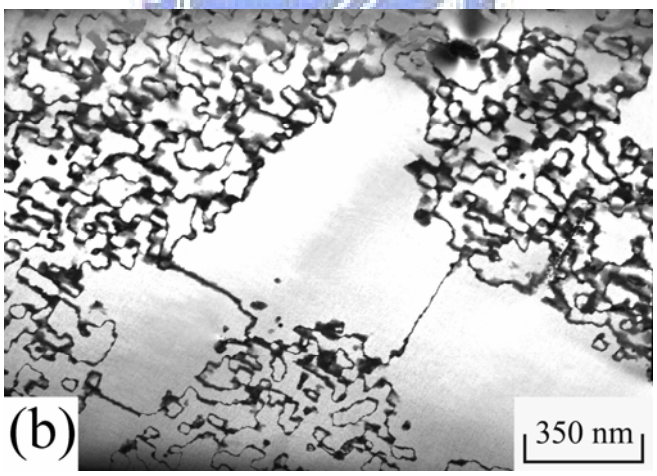

Figure 4.4 (b)

Figure 4.4 ($\bar{1}11$) $D0_3$ DF electron micrographs of the alloy aged at 900˚C for (a) 36 h and (b) 48 h, respectively.

alloy was aged at 900˚C for longer times, phase separation from $D0_3$ to (B2+$D0_3$*) occurred on a/2<100> APBs. This feature has never been reported by other workers in the Fe-Al-Ti alloy systems before. In order to clarify this feature, an STEM-EDS study was undertaken. The EDS analyses were taken from in the middle of $D0_3$ domain (marked as “D”), B2 phase (marked as “B”) and $D0_3$* phase (marked as “D*”) in Figures 4.2 and 4.3(a), respectively. The average concentrations of the alloying elements were obtained from at least ten different EDS profiles of each phase. The results are shown in Table 1. For comparison, the chemical compositions of the as-quenched alloy are also summarized in Table 4.1. It is noted here that since in the present study the EDS analyses were made in the STEM mode on the thin films (not on the extracted phase) and the size of the disordered A2 phase is smaller than that of the electron beam spot (40nm) produced on the JEOL 2000FX STEM. The EDS examination for the disordered A2 phase is not available. It is seen in Table 4.1 that when the alloy was aged at 900˚C for 6 h both the Al and Ti concentrations in the $D0_3$ phase were much greater than those in the as-quenched alloy. It is thus suggested that at this stage, the concentrations of both Al and Ti at a/2<100> APBs would be lacked, which caused the disordered A2 phase to form at a/2<100> APBs. Along

with the growth of the $D0_3$ domains, partial Al and Ti atoms would diffuse toward the a/2<100> APBs. Moreover, when the concentrations of Al and Ti at APBs reached a certain amount, the A2 → B2 transition would occur at a/2<100> APBs. By comparing the chemical compositions of the $D0_3$ domain with $D0_3$* phase in the alloy aged at 900˚C for 24 h, it is evident that the $D0_3$* phase has slightly lower Al content and significantly higher Ti content. Besides, it is well-known that the $D0_3$ phase could only be found in the Fe-Al binary alloys with Al > 25at.% and below 550˚C, and the addition of Ti could increase the $D0_3$ phase field [5]. Obviously, the content of Ti seems to play an important role for the stabilization of the $D0_3$ phase at high temperature. In the present study, EDS analyses indicated that the $D0_3$ phase would separate into the much more stable $D0_3$* phase at 900˚C.

Table 4.1 Chemical Compositions of the Phases Revealed by Energy-Dispersive X-ray Spectrometer (EDS)

Heat Treatment	Phase	Chemical Compositions (at.%)		
		Fe	Al	Ti
as-quenched	A2+$D0_3$	67.9	24.6	7.5
900°C, 6 h	$D0_3$ domain	65.4	26.5	8.1
900°C, 24 h	$D0_3$ domain	66.3	25.5	7.9
	$D0_3$*	65.7	25.2	9.1
	B2	69.3	24.1	6.6

4-4 Conclusions

1. In the as-quenched condition, the microstructure of the Fe-24.6 at.%Al-7.5 at.%Ti alloy was a mixture of (A2+$D0_3$) phases, which was formed by an A2→B2→(A2+$D0_3$) ordering transitions during quenching.
2. When the alloy was aged at 900˚C for moderate times, the $D0_3$ domains grew considerably and B2 phase appeared on a/2<100> anti-phase boundaries (APBs). With continued aging at 900˚C, phase separation from prior-$D0_3$ to (B2+$D0_3$*) occurred initially on a/2<100> APBs, and then proceeded toward the whole prior-$D0_3$ domains. This microstructural revolution has never been reported by other workers in the Fe-Al-Ti alloy systems before.

References

1. F. Stein, A. Schneider, G. Frommeyer, Intermetallics 11 (2003) 71.
2. L. Anthony, B. Fultz, Acta Metall. Mater. 43 (1995) 3885.
3. M. Palm, Intermetallics 13 (2005) 1286.
4. Y. Nishino, S. Asano, T. Ogawa, Mater. Sci. Eng. A 234-236 (1997) 271.
5. M.G. Mediratta, S.K. Ehlers, H.A. Lipsitt, Metall. Trans. A 18 (1987) 509.
6. G. Ghosh, in: G. Effenberg (Eds.), Ternary Alloy Systems, Springer Berlin Heidelberg, New York, 2005, pp. 426-452.
7. I. Ohnuma, C.G. Schön, R. Kainuma, G. Inden, K. Ishida, Acta Mater. 46 (1998) 2083.
8. S.M. Zhu, K. Sakamoto, M. Tamura, K. Iwasaki, Mater. Trans. JIM. 42 (2001) 484.
9. O. Ikeda, I. Ohnuma, R. Kainuma, K. Ishida, Intermetallics 9 (2001) 755.
10. S.M. Allen, J.W. Cahn, Acta Metall. 24 (1976) 425.
11. P.R. Swann, W.R. Duff, R.M. Fisher, Metall. Trans. 3 (1972) 409.
12. C.H. Chen and T.F. Liu: Metall. Trans. A 34 (2003) 503-509.
13. C.H. Chen and T.F. Liu: Scripta Mater. 47 (2002) 515-520.

14. S.Y. Yang and T.F. Liu: Scripta Mater. 54 (2006) 931-935.

15. T.F. Liu, J.S. Chou and C.C. Wu: Metall. Trans. A 21 (1990) 1891-1899.

16. S.Y. Yang and T.F. Liu: J. Alloys Compd. 417 (2006) 63-68.

Chapter 5.

Formation of (B2+$D0_3$) two-phase microstructure in an Fe-23 at.%Al-7 at.%Ti alloy

Formation of (B2+$D0_3$) two-phase microstructure in an Fe-23 at.%Al-7 at.%Ti alloy

Abstract

As-quenched microstructure of the Fe-23 at.% Al-7 at.% Ti alloy was a mixture of (A2+$D0_3$) phases. When the as-quenched alloy was aged at 800˚C for moderate times, $D0_3$ domains grew preferentially along <100> directions and extremely fine B2 particles occurred at a/2<100> anti-phase boundaries (APBs). After prolonged aging at 800˚C, the B2 particles would grow to occupy the whole a/2<100> APBs. Consequently, the stable microstructure of the alloy at 800˚C was a mixture of (B2+$D0_3$) phases.

5-1 Introduction

Effects of Ti addition on the microstructures of the Fe-rich Fe-Al binary alloys have been extensively studied by many workers [1-9]. Based on these studies, it can be generally concluded that the addition of Ti in the Fe-Al binary alloys would not only pronouncedly raise the A2+$D0_3$ (or $D0_3$)→B2→A2 transition temperatures but also significantly expand the (A2+$D0_3$) phase field [3-9]. In addition, a (B2+$D0_3$) two-phase field was reported to be detected in the Fe-Al-Ti ternary alloys [7-9]. Interestingly, the (B2+$D0_3$) two-phase field has not been found by previous workers in the Fe-Al binary alloys before [10-12]. However, to date, the existence of the (B2+$D0_3$) two-phase field in the Fe-Al-Ti ternary alloys was determined principally by means of X-ray diffraction and electron-probe microanalysis (EPMA) [7-9]. Little transmission electron microscopy (TEM) information concerning the formation of the (B2+$D0_3$) two-phase microstructure has been provided in the literature. Therefore, the purpose of this work is an attempt to clarify the microstructural development for the formation of (B2+$D0_3$) phases in the Fe-23 at.% Al-7 at.% Ti alloy by TEM observation.

5-2 Experimental procedure

The Fe-23 at.% Al-7 at.% Ti alloy was prepared in a vacuum induction furnace by using high purity (99.99%) constituent elements. After being homogenized at 1250˚C for 48 h, the ingot was sectioned into 2-mm-thick slices. These slices were subsequently solution heat-treated at 1100˚C for 1 h and then rapidly quenched into room-temperature water. The aging processes were performed at 800˚C for various times in a vacuum heat-treated furnace and then quenched rapidly. TEM specimens were prepared by means of double-jet electropolisher with an electrolyte of 67% methanol and 33% nitric acid. TEM observation of microstructure was performed on a JEOL JEM-2000FX TEM operating at 200kV. This microscope was equipped with a Link ISIS 300 energy-dispersive X-ray spectrometer (EDS) for chemical analysis. Quantitative analyses of elemental concentrations were made with a Cliff-Lorimer Ratio Thin Section method.

5-3 Results and discussion

An optical micrograph of the as-quenched alloy is shown in Figure 5.1(a). Figure 5.1(b) is a selected-area diffraction pattern (SADP) of the as-quenched alloy, exhibiting the superlattice reflection spots of the ordered $D0_3$ phase [13,14]. Figure 5.1(c) is a $(1\bar{1}1)$ $D0_3$ dark-field (DF) electron micrograph, revealing the presence of fine $D0_3$ domains with a/2<100> APBs. Figure 5.1(d), a (200) $D0_3$ DF electron micrograph, shows the presence of small B2 domains with a/4<111> APBs. Since the sizes of both $D0_3$ and B2 domains are small, it is suggested that these domains were formed during quenching [11-17]. In Figure 5.1(d), it is also seen that a high density of disordered A2 phase (dark contrast) was present within the B2 domains; otherwise there would be no dark contrast within these domains by using a (200) superlattice reflection. Therefore, it is concluded that the as-quenched microstructure of the alloy was a mixture of (A2+$D0_3$) phases which were formed by an A2→B2→(A2+$D0_3$) transition during quenching. This result is similar to that reported by Mendiratta *et al.* in the Fe-(18~25)at.% Al-5at.% Ti alloys quenched from 1100˚C [3].

When the as-quenched alloy was aged at 800˚C, the $D0_3$ domains grew rapidly, as illustrated in Figure 5.2. Figure 5.2(a) is a DF electron

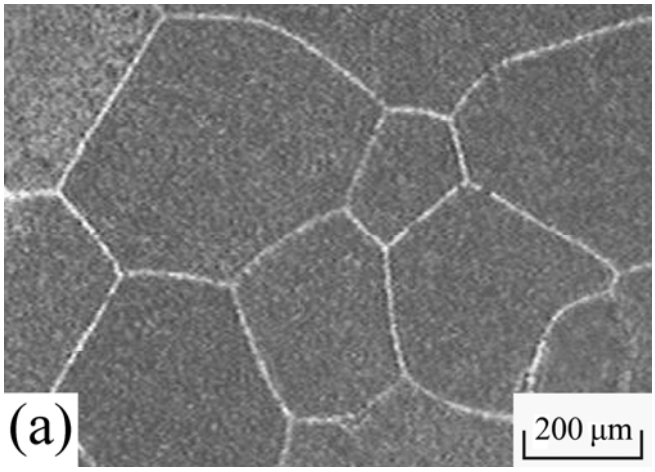

Figure 5.1 (a)

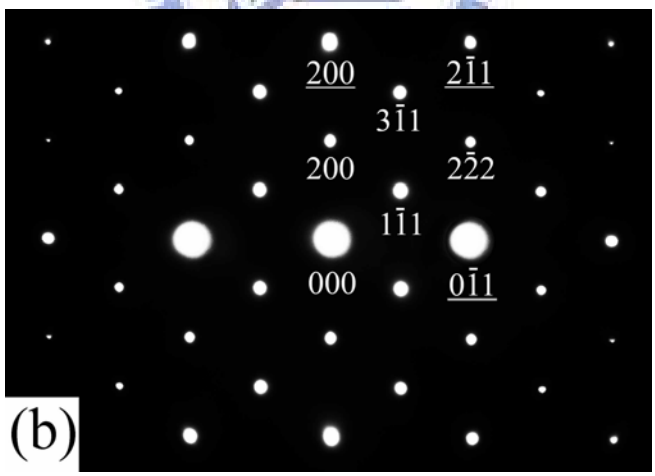

Figure 5.1 (b)

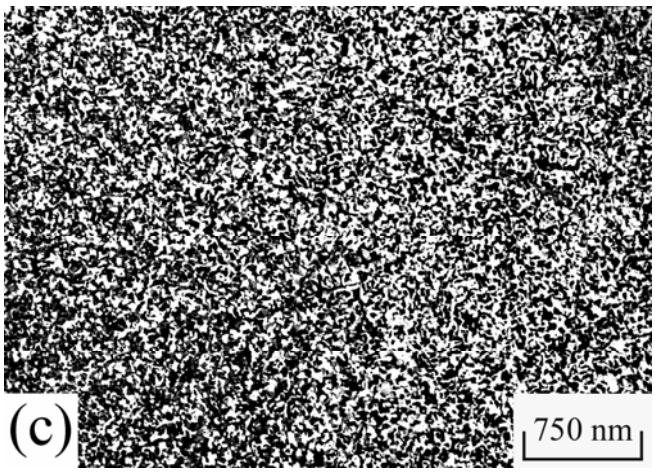

Figure 5.1 (c)

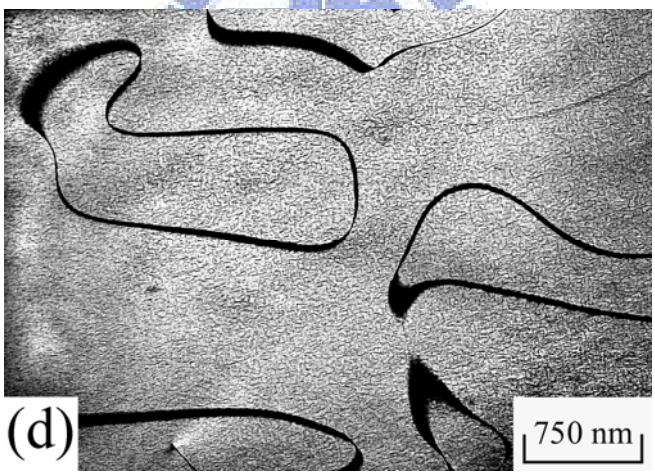

Figure 5.1 (d)

Figure 5.1 (a) An optical micrograph of the as-quenched alloy, (b) through (d) electron micrographs of the as-quenched alloy: (b) an SADP. The foil normal is [011]. (hkl: disordered A2, hkl: $D0_3$ phase.), (c) and (d) $(1\bar{1}1)$ and (200) $D0_3$ DF, respectively.

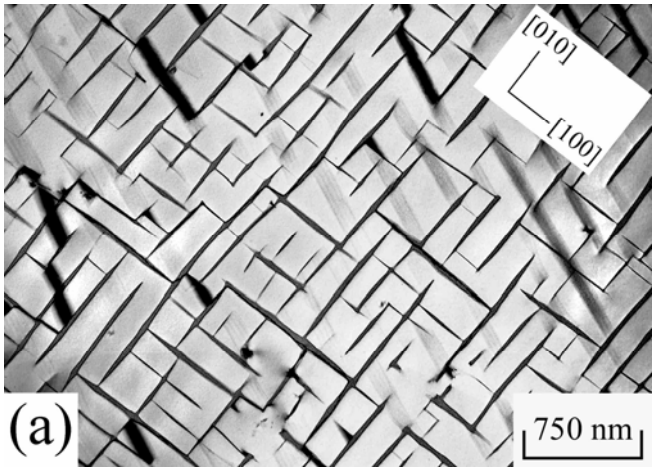

Figure 5.2 (a)

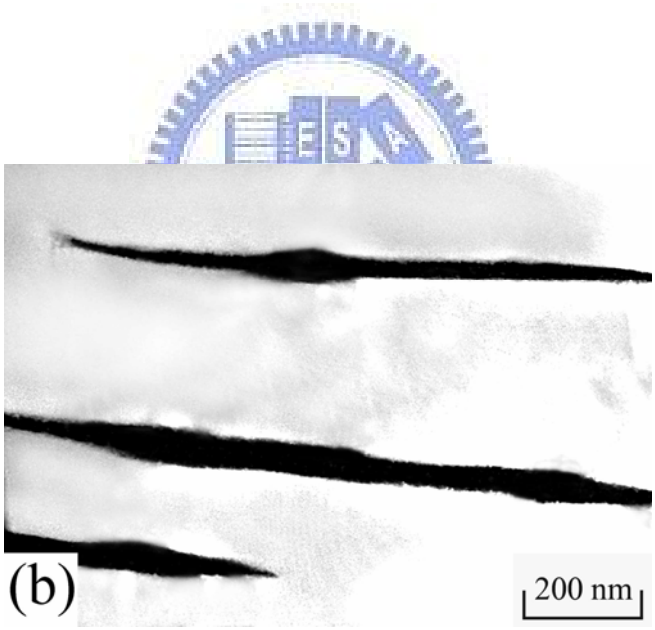

Figure 5.2 (b)

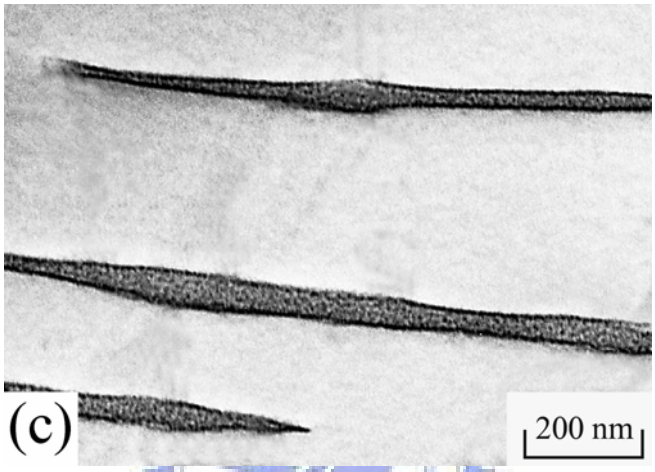

Figure 5.2 (c)

Figure 5.2 Electron micrographs of the alloy aged at 800˚C for 1 h: (a) (200) $D0_3$ DF, (b) and (c) $(1\bar{1}1)$ and (200) $D0_3$ DF with a higher magnification of (a), respectively.

micrograph obtained by use of the (200) superlattice reflection in [001] zone, revealing that the $D0_3$ domains grew preferentially along <100> crystallographic directions. This feature is also similar to that observed by Mendiratta *et al.* [3]. Figure 5.2(b), $(1\bar{1}1)$ $D0_3$ DF electron micrograph of the same area as Figure 5.2(a) with a higher magnification, shows that the a/2<100> APBs are fully dark in contrast. Figure 5.2(b), a (200) $D0_3$ DF electron micrograph, reveals that a high density of extremely fine particles could be observed at the a/2<100> APBs. Since the amount of the particles was very small, the reflection spots of the particles were very faint. In order to carry out an unambiguous identification about the particles, prolonged aging at 800˚C was performed.

Figure 5.3(a) is a bright-field (BF) electron micrograph of the alloy aged at 800˚C for 16 h. In this figure, it is clear that the domains had grown to be very large and the morphology changed from cubic to granular shape. Figures 5.3(b) and 5.3(c) are two SADPs taken from the areas marked as “D” and “B” in Figure 5.3(a), respectively. In our previous study [17], it was found that the intensity of the $(1\bar{1}1)$ and (200) reflection spots of a single $D0_3$ phase should be almost equivalent. Therefore, it seems to be deduced that the reflection spots present in Figure 5.3(b) should be of a single $D0_3$ phase. However, it is clearly seen in Figure

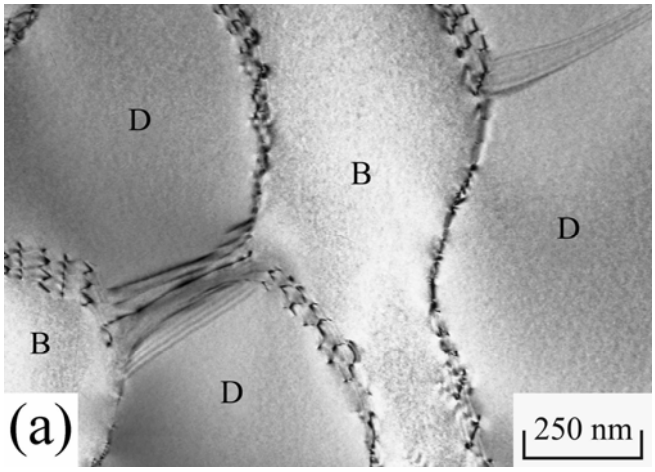

Figure 5.3 (a)

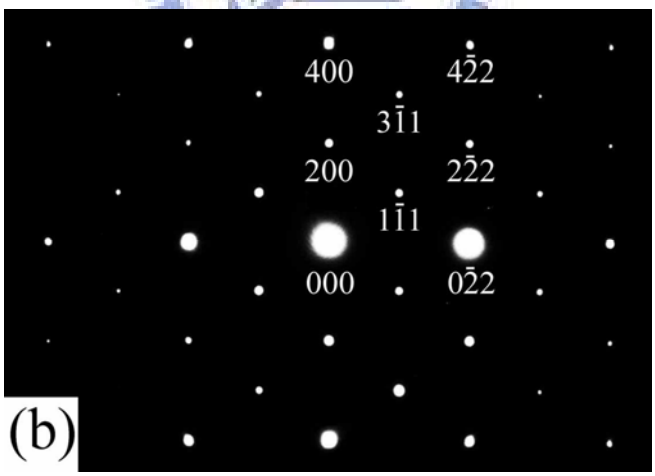

Figure 5.3 (b)

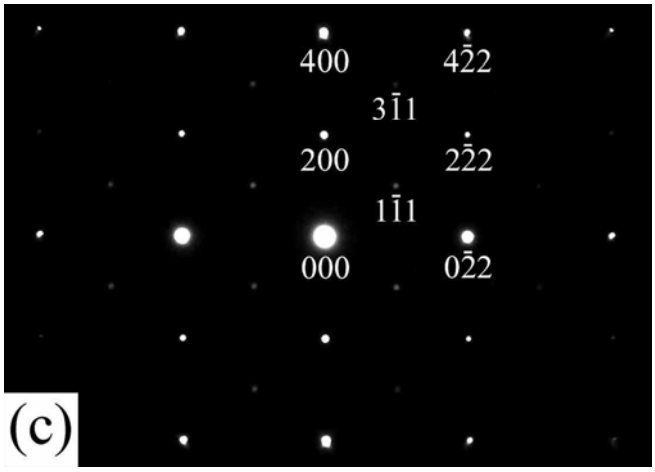

Figure 5.3 (c)

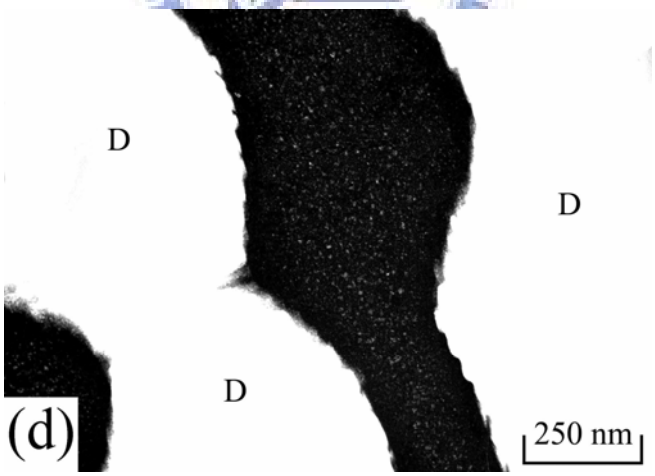

Figure 5.3 (d)

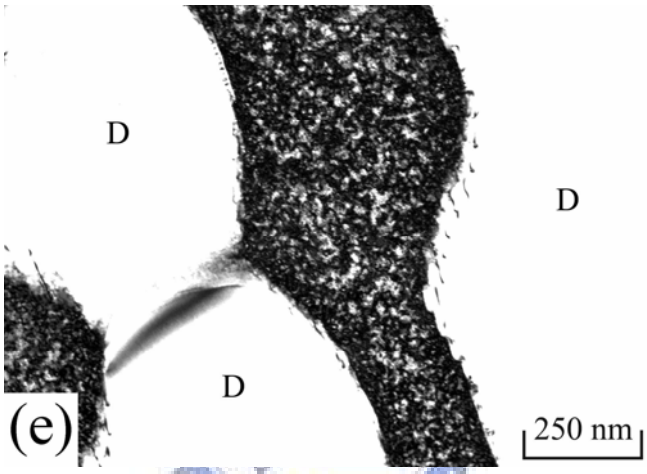

Figure 5.3 (e)

Figure 5.3 Electron micrographs of the alloy aged at 800˚C for 16 h: (a) BF, (b) and (c) two SADPs taken from the areas marked as “D” and “B” in (a), respectively. (*hkl*: $D0_3$ phase), (d) and (e) $(1\bar{1}1)$ and (200) $D0_3$ DF, respectively.

5.3(c) that the (200) and $(2\bar{2}2)$ reflection spots are much stronger than the $(1\bar{1}1)$ reflection spot. Therefore, it is strongly suggested that the (200) and $(2\bar{2}2)$ reflection spots should derive from not only $D0_3$ phase but also the B2 phase, since the $(1\bar{1}1)$ reflection spot comes from the $D0_3$ phase only; while the (200) and $(2\bar{2}2)$ reflection spots can come from both the $D0_3$ and B2 phases (the (200) and $(2\bar{2}2)$ $D0_3$ reflection spots are equal to the (100) and $(1\bar{1}1)$ B2 reflection spots, respectively) [11,12]. Figures 5.3(d) and (e) are $(1\bar{1}1)$ and (200) $D0_3$ DF electron micrographs of the same area as in Figure 5.3(a). It is obviously seen that at the regions marked as "D", the $(1\bar{1}1)$ DF image and the (200) DF image are morphologically identical, and these domains are fully bright in contrast. It means that these domains are of single $D0_3$ phase; whereas, at the regions marked as "B", the B2 particles are much larger than those observed at a/2<100> APBs in Figure 5.2(b), and the $D0_3$ particles are very extremely fine. This indicates that at the regions marked as "B", the B2 particles were existent at the aging temperature, and the extremely fine $D0_3$ particles were formed during quenching from the quenching temperature by a B2→$D0_3$ ordering transition [11-17]. With increasing the aging time at 800˚C, besides the presence of the well-grown $D0_3$ domains, the B2 particles would grow to occupy the whole a/2<100> APBs and

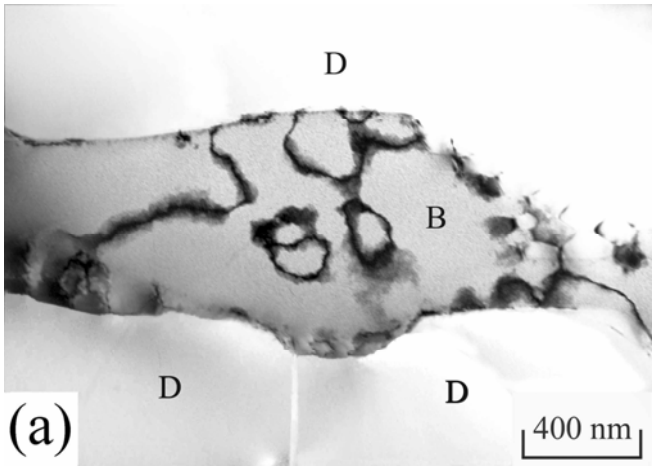

Figure 5.4 (a)

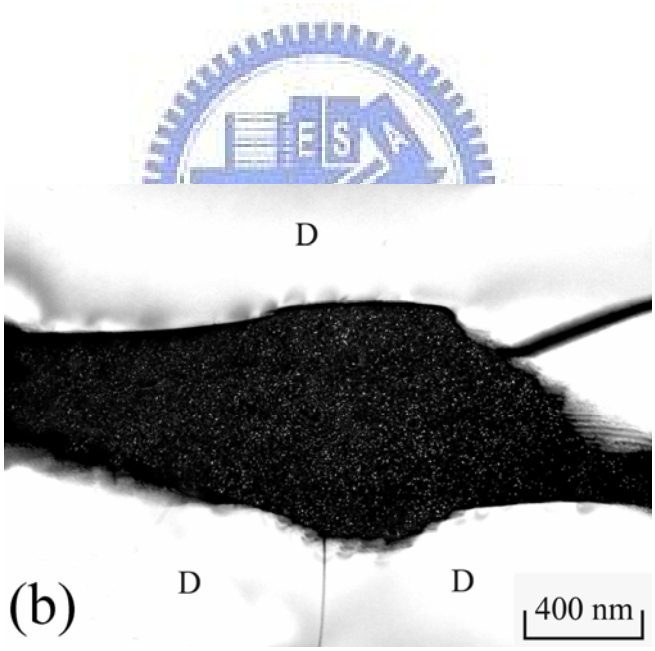

Figure 5.4 (b)

Figure 5.4 (a) and (b) (200) and $(1\bar{1}1)$ $D0_3$ DF electron micrographs of the alloy aged at 800˚C for 72 h.

extremely fine quenched-in $D0_3$ particles could be also detected within the B2 particles. A typical microstructure is illustrated in Figure 5.4. Accordingly, the stable microstructure of the alloy present at 800˚C was a mixture of (B2+$D0_3$) phases.

Based on the preceding results, it is clear that when the present alloy was aged at 800˚C for longer times, the $D0_3$ domains existing in the as-quenched alloy grew and the B2 phase started to occur at the a/2<100> APBs. This transition behavior has never been observed by other workers in the Fe-Al and Fe-Al-Ti alloy systems before. In order to clarify this feature, EDS analyses were undertaken. The average concentrations of the alloying elements were obtained from at least ten different EDS profiles of each phase. The results are summarized in Table 5.1.

Obviously, it is seen in Table 5.1 that both the Al and Ti concentrations in the $D0_3$ phase are much greater than those in the as-quenched alloy. It is thus expected that along with the growth of the $D0_3$ domains, the concentrations of both Al and Ti at a/2<100> APBs would be lacked. The EDS examinations indicated that the elemental concentrations of Al and Ti in the B2 phase are 20.13 and 3.52 at.%, respectively. According to the phase diagram of Fe-Al binary alloys [11,12], it is seen that the

microstructure of an Fe-20.13 at.% Al alloy existing at 800˚C should be a single disordered A2 phase, and no evidence of B2 phase could be observed. Therefore, it is plausible to suggest that the existence of 3.52 at.% Ti at a/2<100> APBs would be favorable for the formation of the B2 phase, rather than the A2 phase.

Finally, it is worthwhile to point out that the B2→$D0_3$ ordering transition could be found to occur in the Fe-Al binary alloys with Al > 25 at.% [12]. However, it is clear in Figure 5.4 that the B2→$D0_3$ ordering transition could be detected and the Al content in the B2 phase was examined to be 20.13 at.% only. This result implies that the existence of Ti would significantly lead the B2→$D0_3$ ordering transition to occur with lower Al content.

Table 5.1 Chemical Compositions of the Phases Revealed by Energy-Dispersive X-ray Spectrometer (EDS)

Heat Treatment	Phase	Chemical Compositions (at.%)		
		Fe	Al	Ti
as-quenched	A2+$D0_3$	69.90	23.08	7.02
900°C, 72 h	$D0_3$	65.76	24.15	10.09
	B2	76.35	20.13	3.52

5-4 Conclusions

1. The as-quenched microstructure of the Fe-23 at.% Al-7 at.% Ti alloy was a mixture of (A2+$D0_3$) phases. The (A2+$D0_3$) phases were formed by an A2→B2→(A2+$D0_3$) transition during quenching.
2. When the alloy was aged at 800˚C for moderate times, the $D0_3$ domains grew preferentially along <100> directions and extremely fine B2 particles occurred at a/2<100> APBs. After prolonged aging at 800˚C, the B2 particles would grow to occupy the whole a/2<100> APBs. Consequently, the stable microstructure of the alloy present at 800˚C was a mixture of (B2+$D0_3$) phases.

References

1. U. Prakash and G. Sauthoff: Intermetallics 9 (2001) 107-112.
2. M. Palm and J. Lacaze: Intermetallics 14 (2006) 1291-1303.
3. M.G. Mediratta, S.K. Ehlers and H.A. Lipsitt: Metall. Trans. A 18 (1987) 509-518.
4. Y. Nishino, S. Asano and T. Ogawa: Mater. Sci. Eng. A 234-236 (1997) 271-274.
5. M. Palm: Intermetallics 13 (2005) 1286-1295.
6. F. Stein, A. Schneider and G. Frommeyer: Intermetallics 11 (2003) 71-82.
7. S.M. Zhu, K. Sakamoto, M. Tamura and K. Iwasaki: Mater. Trans. JIM. 42 (2001) 484-490.
8. I. Ohnuma, C.G. Schön, R. Kainuma, G. Inden and K. Ishida: Acta Mater. 46 (1998) 2083-2094.
9. G. Ghosh: *Ternary Alloy Systems*, (Springer Berlin Heidelberg New York, 2005) pp. 426-452.
10. O. Ikeda, I. Ohnuma, R. Kainuma and K. Ishida: Intermetallics 9 (2001) 755-761.
11. S.M. Allen and J.W. Cahn: Acta Mater. 24 (1976) 425-437.
12. P.R. Swann, W.R. Duff and R.M. Fisher: Metall. Trans. 3 (1972)

409-419.

13. C.H. Chen and T.F. Liu: Metall. Trans. A 34 (2003) 503-509.

14. C.H. Chen and T.F. Liu: Scripta Mater. 47 (2002) 515-520.

15. S.Y. Yang and T.F. Liu: Scripta Mater. 54 (2006) 931-935.

16. T.F. Liu, J.S. Chou and C.C. Wu: Metall. Trans. A 21 (1990) 1891-1899.

17. S.Y. Yang and T.F. Liu: J. Alloys Compd. 417 (2006) 63-68.

Chapter 6.

Phase transformations in an Fe-20 at.% Al-8 at.% Ti alloy

Phase transformations in an Fe-20 at.% Al-8 at.% Ti alloy

Abstract

As-quenched microstructure of the Fe-20 at.% Al-8 at.% Ti alloy was a mixture of (A2+$D0_3$) phases. When the as-quenched alloy was aged at temperatures ranging from 750˚C to 1100˚C, the phase transition sequence as the aging temperature increased was found to be A2+$D0_3$→A2+$D0_3$+C14→B2+C14→A2+C14→A2. It is noted here that this phase transition has never been observed by other workers in the Fe-Al-Ti alloys before.

6-1 Introduction

Efforts to improve the strength of Fe-Al alloy systems at elevated temperatures have been looked for by many workers from the point of the critical temperature T_c for the $D0_3 \rightarrow B2$ transition [1-6]. One of them is the addition of Ti alloying element on the Fe-Al binary alloys [4-6]. According to their reports, the effect of Ti addition on the Fe-Al alloy systems not only increased the $D0_3 \rightarrow B2 \rightarrow A2$ transition temperatures, but also expanded the (A2+ $D0_3$) phase region of the Fe-Al alloy systems. In other word, the limited stability of the $D0_3$ structure can be raised from about 550˚C for binary Fe-Al alloys with 25 at.% Al to approximate 825˚C for adding 5 at.% Ti on the Fe_3Al alloy [6]. As a result, a significant increase in the strength and hardness of Fe-Al-Ti alloys at elevated temperatures was eventually achieved by raising the critical temperature T_c of $D0_3 \rightarrow B2$ transition. In addition, some investigators pointed out that the strength could also be improved due to the precipitation of the hexagonal Fe_2Ti with C14 phase [7-9]. Previous studies have shown that when Ti content increased greater than 7 at.%, the C14 phase could start to precipitate at grain boundaries and within grains [10].

In the previous studies [6], it is clearly seen that although the phase transformations in the Fe-Al-Ti alloys have been studied, most of the

examinations were only focused on the Fe-Al-Ti alloys with lower Ti content. Information concerning the microstructural development of the Fe-Al-Ti alloys with higher Ti content is very insufficient. Therefore, the purpose of the present study is to investigate the as-quenched microstructures of the Fe-Al-Ti alloys with Ti > 7 at.%.

6-2 Experimental procedure

The Fe-20 at.% Al-8 at.% Ti alloy was prepared in a vacuum induction furnace by using high purity (99.99%) constituent elements. After being homogenized at 1250˚C for 48 h, the ingot was sectioned into 2-mm-thick slices. These slices were subsequently solution heat-treated at 1250˚C for 1 h and then rapidly quenched into room-temperature water. The aging processes were performed at temperatures ranging from 750˚C to 1100˚C in a vacuum heat-treated furnace for various times and then quenched into room-temperature water rapidly. TEM specimens were prepared by means of double-jet electropolisher with an electrolyte of 67% methanol and 33% nitric acid. TEM observation of microstructure was performed on a JEOL JEM-2000FX TEM operating at 200kV. This microscope was equipped with a Link ISIS 300 energy-dispersive X-ray spectrometer (EDS) for chemical analysis. Quantitative analyses of elemental concentrations were made with a Cliff-Lorimer Ratio Thin Section method.

6-3 Results and discussion

Figure 6.1(a) is a bright-field (BF) electron micrograph of the as-quenched alloy. Figure 6.1(b) is a selected-area diffraction pattern (SADP) of the as-quenched alloy, exhibiting the superlattice reflection spots of the ordered $D0_3$ phase [11]. Figure 6.1(c) is a $(\bar{1}11)$ $D0_3$ dark-field (DF) electron micrograph of the as-quenched alloy, revealing the presence of extremely fine $D0_3$ domains. Figure 6.1(d), a (002) $D0_3$ DF electron micrograph, shows the presence of small B2 domains with a/4<111> APBs. Since the sizes of both $D0_3$ and B2 domains are very small, it is suggested that these domains were formed by ordering transition during quenching. In Figure 6.1(d), it is also seen that a very high density of disordered A2 phase (dark contrast) was present within the B2 domains. It is concluded from the above observations that in the as-quenched condition, the microstructure of the alloy was a mixture of (A2+$D0_3$) phases, which were formed by an A2→B2→(A2+$D0_3$) ordering transition during quenching [12-19]. This result is similar to that observed by other workers in the Fe-(18~22.5) at.% Al-5 at.% Ti alloys [6].

When the as-quenched alloy was aged at 750˚C, the $D0_3$ domains grew, as illustrated in Figure 6.2. Figure 6.2 is a DF electron micrograph obtained by use of the (200) superlattice reflection in [001] zone,

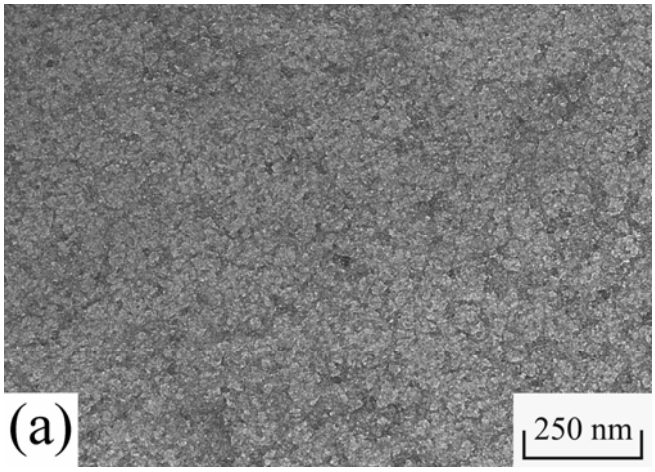

Figure 6.1 (a)

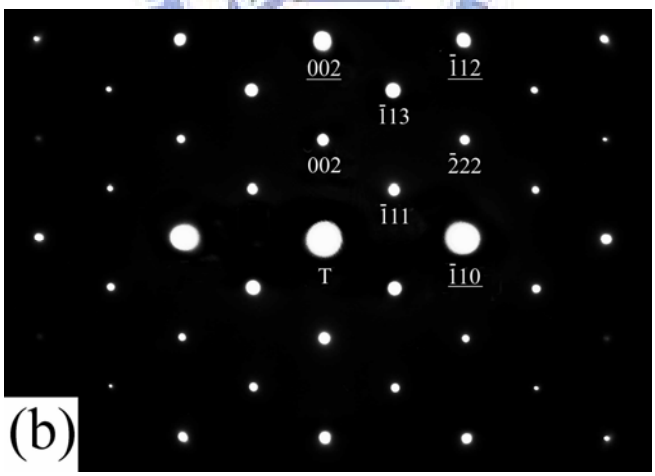

Figure 6.1 (b)

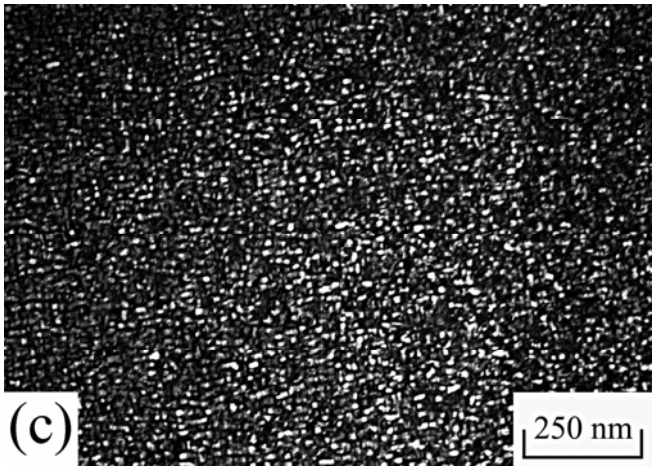

Figure 6.1 (c)

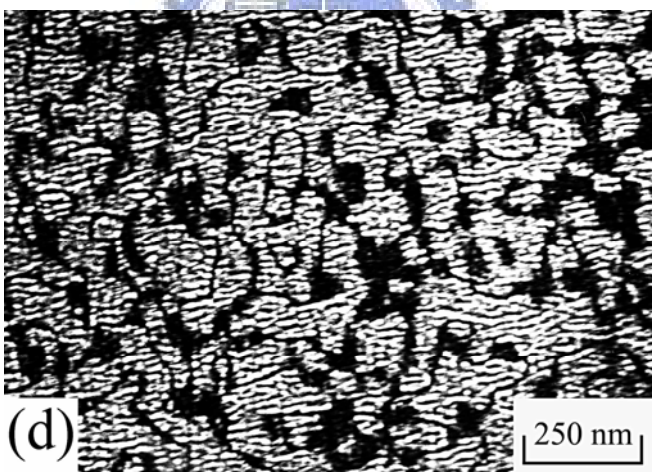

Figure 6.1 (d)

Figure 6.1 Electron micrographs of the as-quenched alloy: (a) BF, (b) an SADP. The foil normal is [110]. (<u>hkl</u> = ferrite phase; hkl = $D0_3$ phase.), (c) and (d) ($\bar{1}11$) and (002) $D0_3$ DF, respectively.

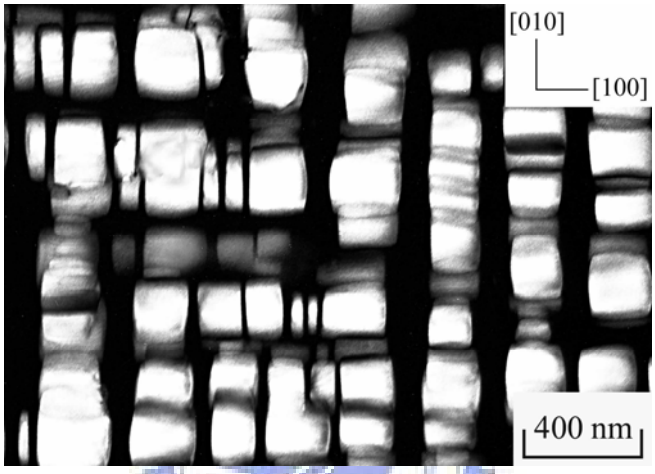

Figure 6.2

Figure 6.2 (200) $D0_3$ DF electron micrograph of the alloy aged at 750˚C for 1 h.

revealing that the $D0_3$ domains were formed lying along <100> directions. This feature is also similar to that observed by Mendiratta *et al.* in the aged Fe-Al-Ti alloys [6]. With increasing the aging time at 750˚C, the $D0_3$ domains continued to grow and the morphology changed from cubic to granular shape, as illustrated in Figure 6.3. Figures 6.3(a) and (b) are $(\bar{1}11)$ and (002) $D0_3$ DF electron micrographs, clearly showing that the $(\bar{1}11)$ and (002) $D0_3$ DF are morphologically identical. Since the (002) reflection spot comes from both the B2 and $D0_3$ phases, while the $(\bar{1}11)$ reflection spot comes only from $D0_3$ phase, the bright particles presented in Figures 6.3(a) and (b) are considered to be $D0_3$ phase, not B2 phase. This result indicates that the microstructure of the alloy present at 750˚C was a mixture of (A2+$D0_3$) phases. Figure 6.4(a) is a bright-field (BF) electron micrograph of the alloy aged at 850˚C for 1 h. In this figure, it is clear that some rod-like precipitates were found to appear within the matrix. Figures 6.4(b) through (d) demonstrate three different SADPs taken from an area including the precipitate marked as “C” in Figure 6.4(a) and its surrounding matrix. The crystallographic normals of the (A2+$D0_3$) matrix are $[1\,1\,1]_m$, $[1\,1\,0]_m$ and $[\bar{1}\,\bar{1}\,2]_m$, respectively. In addition to the reflection spots corresponding to the (A2+$D0_3$) phases, the diffraction patterns also consist of small spots caused by the presence of the

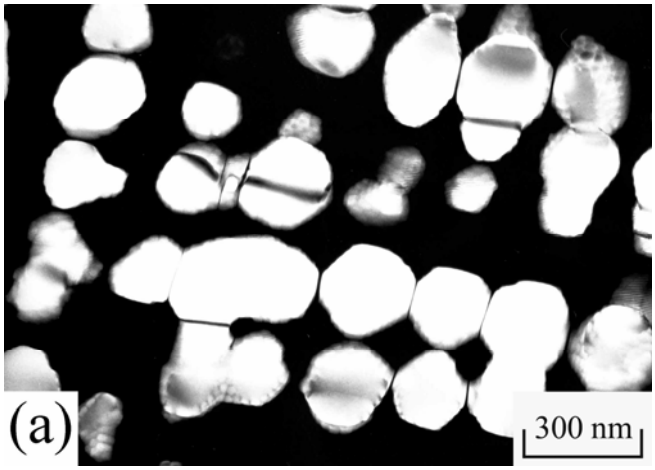

Figure 6.3 (a)

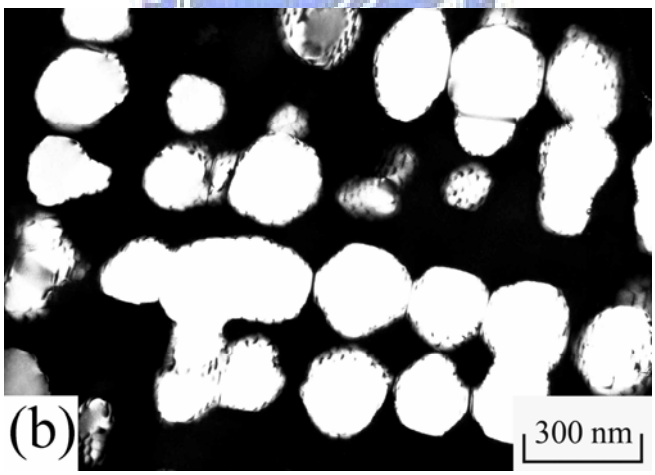

Figure 6.3 (b)

Figure 6.3 Electron micrographs of the alloy aged at 750˚C for 12 h: (a) and (b) $(\bar{1}11)$ and (002) $D0_3$ DF, respectively.

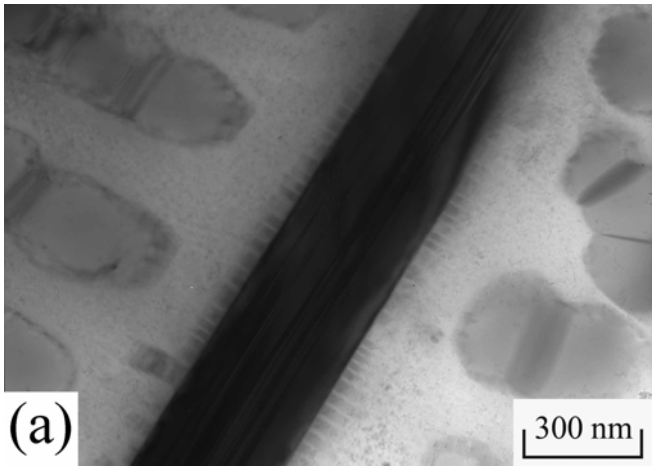

Figure 6.4 (a)

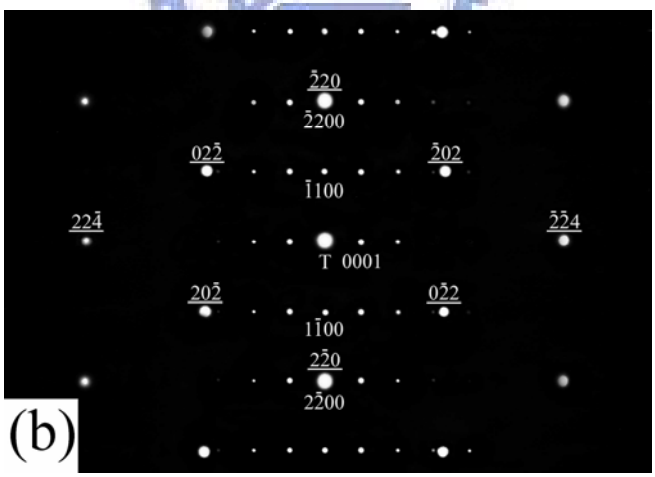

Figure 6.4 (b)

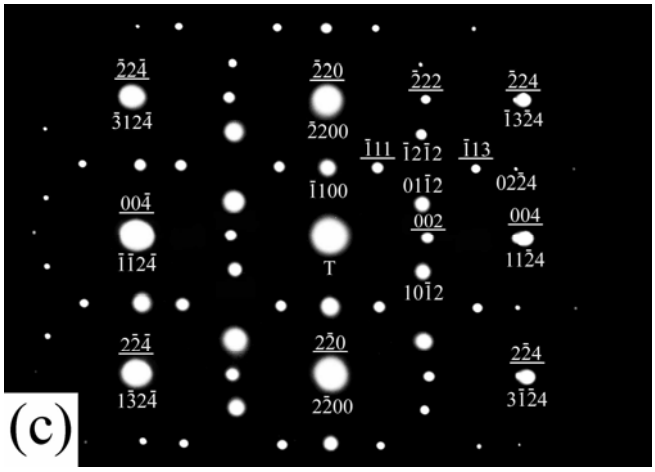

Figure 6.4 (c)

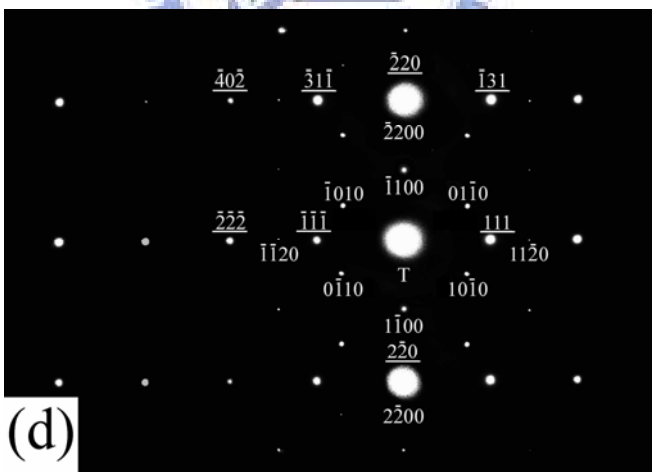

Figure 6.4 (d)

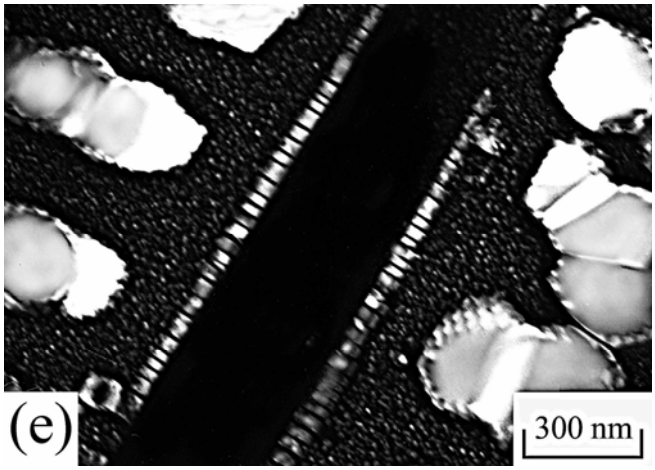

Figure 6.4 (e)

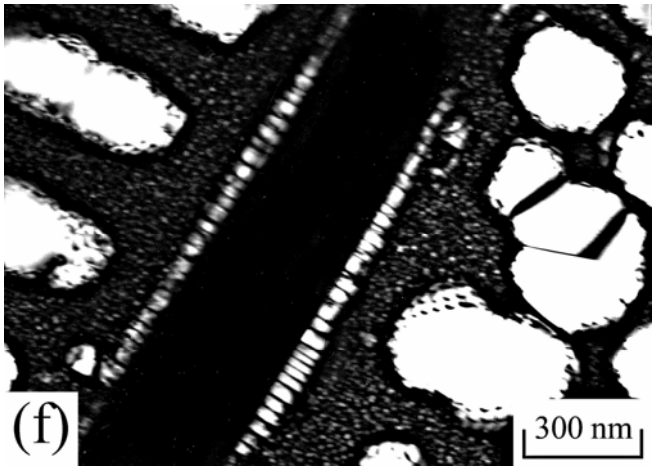

Figure 6.4 (f)

Figure 6.4 Electron micrographs of the alloy aged at 850˚C for 1 h: (a) BF, (b) through (d) three SADPs taken from an area including the C14 precipitate and its surrounding matrix. The zone axes of the (A2+$D0_3$) matrix are (b) $[1\,1\,1]$, (c) $[1\,1\,0]$, (d) $[\bar{1}\,\bar{1}\,2]$, respectively. (hkil = C14 precipitate; <u>hkl</u> = $D0_3$ phase), (e) and (f) $(\bar{1}11)$and $(002)$$D0_3$ DF, respectively.

precipitate. According to the camera length and the measurement of angles as well as d-spacings of the diffraction spots, the crystal structure of the precipitate phase was determined to be hexagonal with lattice parameters a=0.505 nm and c=0.801 nm, which corresponds to that of the C14 phase [20]. Analyses by the above diffraction patterns, the orientation relationship between the C14 precipitate and (A2+$D0_3$) matrix was determined to be $(0\,0\,0\,1)_{C14}//(\bar{1}\,\bar{1}\,2)_m$, $(\bar{1}\,1\,0\,0)_{C14}//(\bar{1}\,1\,0)_m$, $(1\,1\,\bar{2}\,0)_{C14}//(1\,1\,1)_m$. It is worthy mentioning that the orientation relationship between the C14 precipitate and A2, $D0_3$ or B2 matrix has never been reported by other workers in the Fe-Al-Ti alloy systems before. Figures 6.4(e) and (f) are $(\bar{1}11)$ and (002) $D0_3$ DF electron micrographs, clearly revealing that three types of $D0_3$ particles could be detected: one is the granular-like $D0_3$ particles within the matrix; another is the cuboidal $D0_3$ particles contiguous to the C14 precipitate. Since the sizes of these two types of $D0_3$ particles are larger than those observed in the as-quenched alloy. It is therefore reasonable to believe that these two types of the $D0_3$ particles were existent at the aging temperature. The other is the extremely fine $D0_3$ particles within the A2 matrix, which were formed during quenching. It is concluded from the above observations that the microstructure of the alloy present at 850˚C was a mixture of

(A2+$D0_3$+C14).

Shown in Figure 6.5(a) is $(\bar{1}11)$ $D0_3$ DF electron micrograph of the alloy aged at 900˚C for 1 h and then quenched. It reveals that the extremely fine $D0_3$ domains with a/2<100> APBs could be observed. The size of the $D0_3$ domains is very small, indicating that the extremely fine $D0_3$ domains were formed during quenching from the aging temperature; otherwise, its size should be increased at the aging temperature. Figure 6.5(b), a (002) $D0_3$ DF electron micrograph of the same area as Figure 6.5(a), shows that along with growth of the B2 domains, the a/4<111> APBs had gradually disappeared. Furthermore, it is also seen that the disordered A2 phase with a dark contrast could be observed within the B2 domains. This indicates that the matrix present at 900˚C should be B2 phase and the extremely fine $D0_3$ domains were formed by a B2→(A2+$D0_3$) ordering transition during quenching. Accordingly, the microstructure of the present alloy at 900˚C was a mixture of (B2+C14) phases. However, when the alloy was aging at 950˚C for 1 h and then quenched, the $(\bar{1}11)$ and (002) $D0_3$ DF electron micrographs revealed that in addition to C14 precipitates, only quenched-in extremely fine $D0_3$ domains and small B2 domains were present within the matrix. An example is illustrated in Figure 6.6. This means that the stable

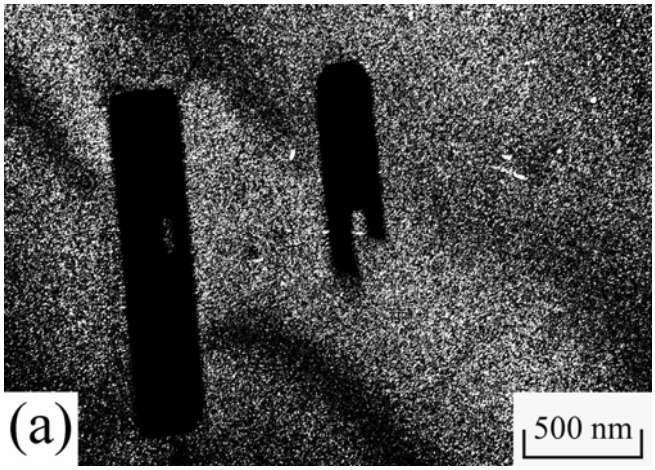

Figure 6.5 (a)

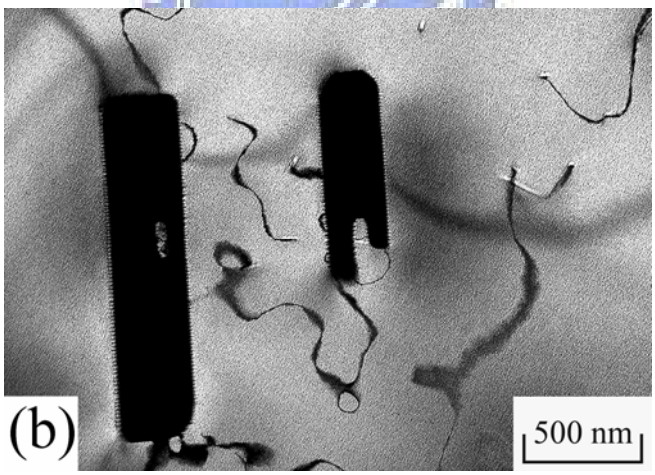

Figure 6.5 (b)

Figure 6.5 Electron micrographs of the alloy aged at 900˚C for 1 h: (a) and (b) ($\bar{1}11$) and (002) $D0_3$ DF, respectively.

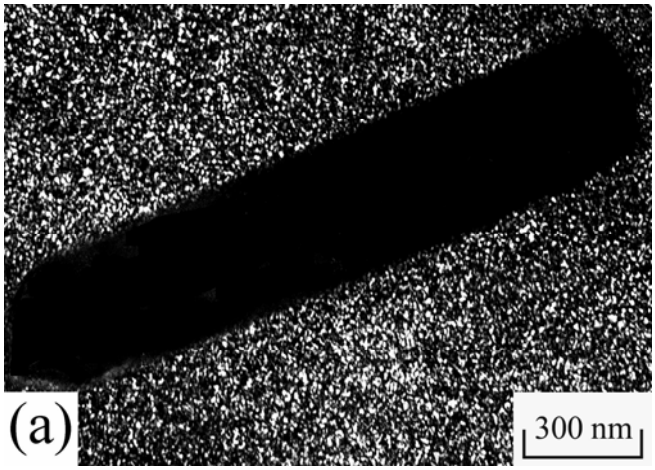

Figure 6.6 (a)

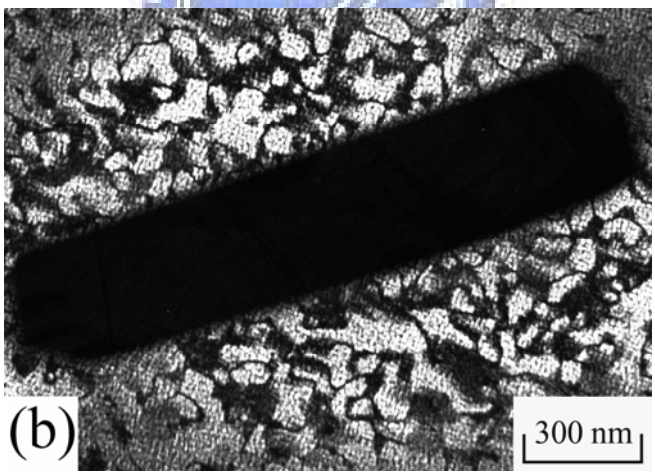

Figure 6.6 (b)

Figure 6.6 Electron micrographs of the alloy aged at 950˚C for 1 h: (a) and (b) $(\bar{1}11)$ and (002) $D0_3$ DF, respectively.

microstructure of the present alloy at 950˚C was a mixture of (A2+C14) phases.

Progressively higher temperature aging and quenching experiments indicated the mixture of (A2+C14) phases could be preserved up to 1050˚C. However, when the alloy was aged at 1100˚C and then quenched, the C14 precipitates disappeared and only quenched-in small B2 domains (the size being comparable to that observed in the as-quenched alloy) could be detected, as illustrated in Figure 6.7. This indicates that the microstructure of the present alloy existing at 1100˚C or above should be the single disordered A2 phase. It is therefore concluded that with increasing the aging temperature from 750˚C to 1100˚C, the phase transition sequence in the present alloy was A2+$D0_3$→A2+$D0_3$+C14→B2 +C14→A2+C14→A2.

Based on the above observations, two important features of the present study are worthy to note as follows: (Ⅰ) When the present alloy was aged at 850˚C, the cuboidal $D0_3$ particles could be observed to form contiguous to the C14 precipitates. It is a remarkable feature in the present study, which has never been observed by others in the Fe-Al-Ti alloy systems before. In order to clarify this feature, an STEM-EDS study was made. Figures 6.8(a) through (d) represent four typical EDS spectra

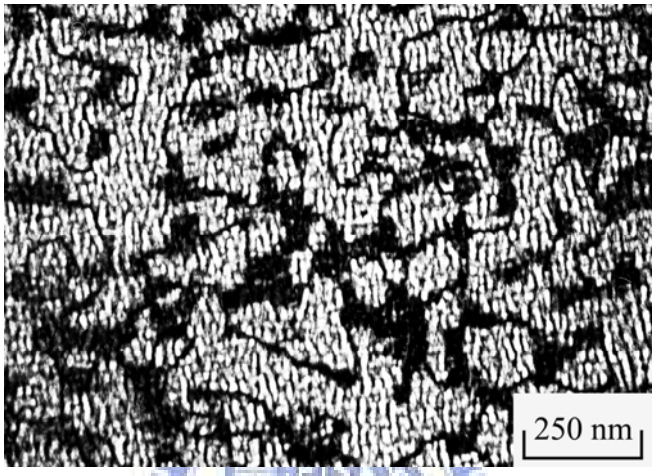

Figure 6.7

Figure 6.7 (002) $D0_3$ DF electron micrograph of the alloy aged at 1100˚C for 1 h.

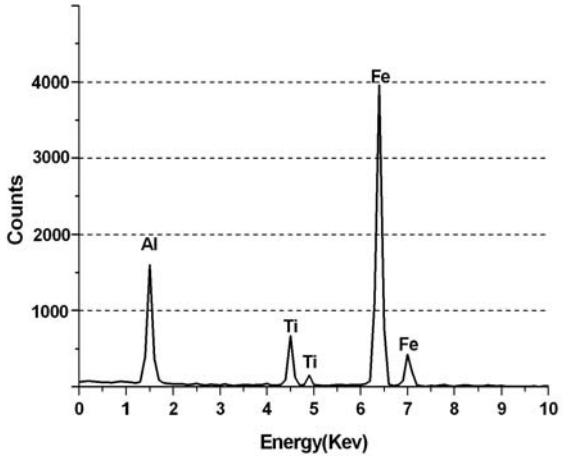

Figure 6.8 (a)

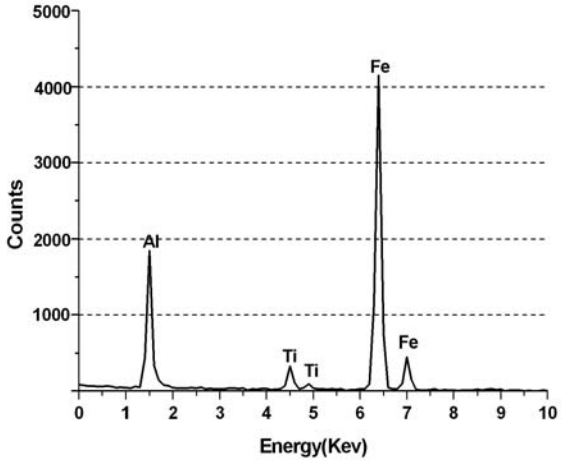

Figure 6.8 (b)

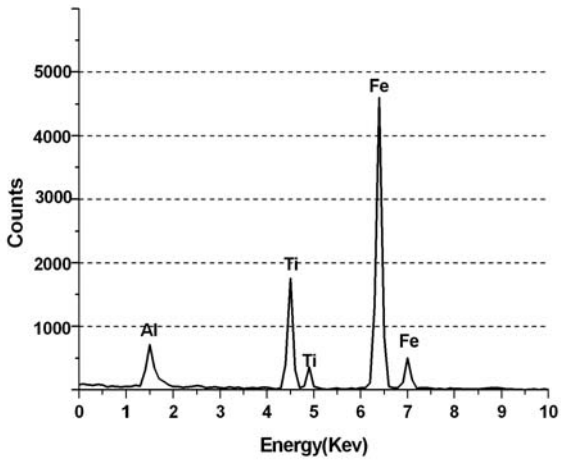

Figure 6.8 (c)

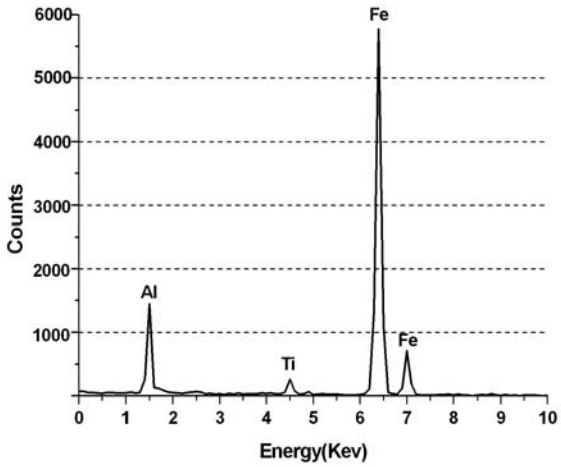

Figure 6.8 (d)

Figure 6.8 (a) through (d) four typical EDS spectra taken from a granular-like $D0_3$ particle within the matrix, a cuboidal $D0_3$ particle contiguous to the C14 precipitate, C14 precipitate and the ($A2+D0_3$) matrix in the alloy aged at 850˚C for 1 hour, respectively.

taken from a granular-like $D0_3$ particle within the matrix, a cuboidal $D0_3$ particle contiguous to the C14 precipitate, C14 precipitate and the (A2+$D0_3$) matrix in the alloy aged at 850˚C for 1h, respectively. The average concentrations of alloying elements obtained by analyzing a number of EDS spectra of each phase are listed in Table 6.1. For comparison, the chemical compositions of the as-quenched alloy are also listed in Table 6.1. The quantitative analyses revealed that the atomic percentages of the alloying elements in the C14 precipitate and cuboidal $D0_3$ particle were Fe-9.4at.% Al-25.7 at.% Ti and Fe-25.9 at.% Al-6.3 at.% Ti. It is clear that the concentration of Ti in the C14 precipitate is much higher than that in the as-quenched alloy and the concentration of Al is obviously lower than that in the as-quenched alloy. However, it is seen in Figure 6.8(b) and Table 6.1 that Al concentration in the cuboidal $D0_3$ particles is much higher than C14 precipitate and (A2+$D0_3$) matrix. Therefore, it is expected that along with the precipitation of C14 phase, the surrounding regions would be enriched in Al. The enrichment in Al would cause the Al-rich $D0_3$ particles to form at the regions contiguous to the C14 precipitates, as observed in Figure 6.4(e). (Ⅱ) It is well-known that the $D0_3$ phase could be formed by ordering transition during quenching with Al > 20 at.% in the Fe-Al binary alloys [13]. However, it is

clear in Figure 6.4(e) that the A2→A2+$D0_3$ ordering transition could be detected and the Al content in the A2 phase was examined to be 17.9 at.% only. Therefore, it is believed that the solubility of 4.9 at.% Ti within the A2 phase would enhance the A2→A2+$D0_3$ ordering transition to occur during quenching. (Ⅲ) Recently, Morris *et al.*, reported that when the Fe-25 at.% Al-2 at.% Nb alloy was aged at 800˚C, C14 precipitates were formed within the $D0_3$ matrix and the orientation relationship between the C14 precipitate and $D0_3$ matrix was $\{\bar{1}010\}_{C14}//\{\bar{1}01\}_m$, $<1\bar{2}10>_{C14}\approx<010>_m$ and $<0001>_{C14}\approx<101>_m$ [21]. Accordingly, Morris *et al.* claimed that the only exact relationship was $\{\bar{1}010\}_{C14}//\{\bar{1}01\}_m$ and all other relationships were approximate with a difference of a few degrees (3~5˚). Compared with present work, it is worthy to note here that only $(\bar{1}100)_{C14}//(\bar{1}10)_m$ is indeed in agreement with Morris *et al.*, but the other relationships are discrepant.

Table 6.1 Chemical Compositions of the Phases Revealed by Energy-Dispersive X-ray Spectrometer (EDS)

Heat Treatment	Phase	Chemical Compositions (at.%)		
		Fe	Al	Ti
as-quenched	A2+$D0_3$	71.7	20.2	8.1
850°C, 1 h	granular-like $D0_3$	65.4	23.2	11.4
	cuboidal $D0_3$	67.8	25.9	6.3
	C14	64.9	9.4	25.7
	A2+$D0_3$	77.2	17.9	4.9

6-4 Conclusions

1. The as-quenched microstructure of the Fe-20 at.% Al-8 at.% Ti alloy was a mixture of (A2+$D0_3$) phases. The (A2+$D0_3$) phases were formed by an A2→B2→(A2+$D0_3$) ordering transition during quenching.
2. When the alloy was aged at 750˚C, the $D0_3$ precipitates grew lying along <100> directions. With increasing aging time, the $D0_3$ domains continued to grow and the morphology changed from cuboidal to granular shape.
3. When the alloy was aged at 850˚C for 1 h, the rod-like C14 precipitates could be observed within the (A2+$D0_3$) matrix. Along with the growth of the C14 precipitates, the surrounding region would be enriched in aluminum. The enrichment of aluminum would enhance the formation of the cuboidal $D0_3$ particles at the regions contiguous to the C14 precipitates.
4. When the as-quenched alloy was aged at temperatures ranging from 750˚C to 1100˚C, the phase transformation sequence as the aging temperature increased was found to be (A2+$D0_3$) → (A2+$D0_3$+C14) → (B2+C14) → (A2+C14) → A2.
5. The orientation relationship between the C14 precipitate and (A2+$D0_3$)

matrix was determined to be $(0001)_{C14}//(\bar{1}\bar{1}2)_m$, $(\bar{1}100)_{C14}//(\bar{1}10)_m$, $(11\bar{2}0)_{C14}//(111)_m$, which has never been reported in the Fe-Al-Ti alloy systems before.

References

1. J. M. Cairney, P. R. Munroe, J. Mater. Sci. Letters 18 (1999) 449.
2. U. Prakash, R.A. Buckley, H. Jones, Mater. Sci. Tech. 9 (1993) 16.
3. Y. Nishino, S. Asano, T. Ogawa, Mater. Sci. Eng. A 234-236 (1997) 271.
4. L. Anthony, B. Fultz, Acta metall. mater. 43 (1995) 3885.
5. Y. Nishino, C. Kumada, S. Asano, Scripta Mater. 36 (1997) 461.
6. M.G. Mediratta, S.K. Ehlers, H.A. Lipsitt, Metall. Trans. A 18 (1987) 509.
7. M. Palm, Intermetallics 13 (2005) 1286.
8. F. Stein, M. Plam, G. Sauthoff, Intermetallics 13 (2005) 1056.
9. F. Stein, M. Plam, G. Sauthoff, Intermetallics 13 (2004) 713.
10. C.H. Sellers, T.A. Hyde, T.K. O'Brien, R.N. Wright, J. Phys. Chem. Solids 55 (1994) 505.
11. C.H. Chen, T.F. Liu, Metall. Trans. A 34 (2003) 503.
12. S.M. Allen and J.W. Cahn: Acta Mater. 24 (1976) 425-437.
13. P.R. Swann, W.R. Duff and R.M. Fisher: Metall. Trans. 3 (1972) 409-419.
14. C.H. Chen and T.F. Liu: Scripta Mater. 47 (2002) 515-520.
15. S.Y. Yang and T.F. Liu: Scripta Mater. 54 (2006) 931-935.

18. T.F. Liu, J.S. Chou and C.C. Wu: Metall. Trans. A 21 (1990) 1891-1899.

19. S.Y. Yang and T.F. Liu: J. Alloys Compd. 417 (2006) 63-68.

20. M. Palm, G. Inden, N. Thomas, J. Phase Equilibria 16 (1995) 209.

21. D.G. Morris, L.M. Requejo, M.A. Muñoz-Morris, Intermetallics 13 (2005) 862.

List of Publications

- **Journal Papers**

1. C.W. Su, S.C. Jeng, C.G. Chao and T.F. Liu, "Orientation relationship between C14 precipitate and ferrite matrix in an Fe-20 at.% Al-8 at.% Ti alloy", accepted for publication in Scripta Mater. (2007,3)
2. C.W. Su, C.G. Chao and T.F. Liu, "Formation of (B2+$D0_3$) Phases at a/2<100> anti-phase boundary in an Fe-23 at.% Al-8.5 at.% Ti alloy", accepted for publication in Scripta Mater. (2007,7)
3. C.W. Su, L.W. Lee, C.S. Wang, C.G. Chao and T.F. Liu, "The effect of hot-dipped aluminum coatings on Fe-8Al-30Mn-0.8C alloy", accepted for publication in Surface and Coatings Technology. (2007,8)
4. C.W. Su, C.G. Chao and T.F. Liu, "Formation of (B2+$D0_3$) two-phase microstructure in a Fe-23 Al-7 Ti alloy", accepted for publication in Mater. Trans., JIM (2007,8)
5. C.W. Su, C.G. Chao and T.F. Liu, "Phase separation from $D0_3$ to (B2+ $D0_3$) in an Fe-24.5 at.% Al-7.6 at.% Ti alloy", submitted to J. Alloy. Compd.
6. C.W. Su, C.G. Chao and T.F. Liu, "Phase transformations in an Fe-20

at.% Al-8 at.% Ti alloy", submitted to Intermetallics.

- **Conferences Papers**

1. C.W. Su, Z.L. Lin, Z.L. Liu, X.L. Lin, T.F. Liu "Orientation relationship between C14 precipitate and ferrite matrix in an Fe-20 at.% Al-8 at.% Ti alloy", Proceedings of The 2007 Annual Conference of The Chinese Society for Materials Science (2007)
2. 王承舜, 曾傑享, 蘇俊瑋, 林志龍, 陳信良, 劉增豐 "鐵-9 鋁-30 錳-1.6 碳合金顯微結構與機械性質", Proceedings of The 2005 Annual Conference of The Chinese Society for Materials Science (2005)

   (榮獲中國材料科學學會材料科學學生論文獎優等獎)
3. 李堅瑋, 蘇俊瑋, 段逸軒, 劉增豐 "熱浸鍍鋁鐵鋁錳碳合金之研究", Proceedings of The 2003 Annual Conference of The Chinese Society for Materials Science OA-006 (2003)